THE UNIVERSITY
OF BIRMINGHAM

MAGNETIC RESONANCE IMAGING OF COPPER CORROSION

By

Ismaila Abdullahi

A thesis submitted to

the University of Birmingham

for the degree of

MASTERS BY RESEARCH

School of Chemistry

College of Engineering and Physical Sciences

The University of Birmingham

August 2013

Abstract

This research project studied the corrosion of copper in 0.5 M sodium chloride and 1.5 % w/v agar using magnetic resonance imaging (MRI).

The imaging artefacts frequently associated with metals in the MRI were minimised in the copper corrosion system by aligning the copper strip in the cell parallel to the radio-frequency field of the spectrometer.

T_1 and T_2 relaxation measurements of varying copper concentrations in 0.5 M sodium chloride and 1.5 % w/v agar show that the relaxation rate of proton water molecules increase with increasing copper concentration in the control samples. Diamagnetic contributions from other species apart from copper ions to the relaxivity of proton water molecules in the system were also observed.

MRI was used to map spatial distribution and concentration of copper ions in electrolyte solution of sodium chloride for the first time. A time series of T_2 maps of the system show reduction in spin-spin relaxation times during the corrosion process, which was attributed to increase in the concentration of copper ions in the electrolyte solution near the metal. Also, a time series of T_2 maps revealed the spatial distribution of copper ions during the process of copper corrosion. The T_2 concentration maps also showed how the concentration of copper ions increases as they are spatially distributed during the process. A time series of T_1 maps does not show any significant variation in T_1 times during the corrosion process. This was attributed to the corrosion products formed in the system.

Dedication

This work is dedicated to my parents, late Aishatu Abdullahi and Abdullahi Mari.

Acknowledgments

First and foremost I would like to thank Allah (SWT) for sparing my life up to this time and for giving me the health and wisdom to carry out this research.

My utmost appreciation goes to the tertiary education trust fund, Nigeria (TERTFUND), for funding my studies and my employer, University of Abuja, Nigeria for granting me study leave.

I would like to thanks my supervisor, Melanie Britton for supervising this work. The contribution of the MRI group must also be acknowledged especially Antoine and Amanda. I would also like to thank members of the computational chemistry group especially Chris and Charlotte for their kindness and warmth friendship.

The support of all my friends here in Birmingham must also be acknowledged. I would like to thank Bala, Auwalu, Aminu, Akilu, Misbahu, Selina, Fabian, Mariwan and so many others whose names I cannot remember.

Finally, my sincere appreciation goes to my Dad, Abdullahi Mari, my lovely wife Khadija and my siblings, Mariya, Ibrahim, sadiq, yanbiyu, Suwaiba, Fatima and Abdulkadir for their support, prayers and understanding throughout the period of my studies.

List of abbreviations

CPMG – Carr-Purcell-Meiboom-Gill

FID – Free Induction Decay

MRI – Magnetic Resonance Imaging

NMR – Nuclear magnetic Resonance

RARE – Rapid Acquisition with Relaxation Enhancement

rf – Radiofrequency

Table of Contents

1 Introduction

Magnetic resonance imaging (MRI), which is commonly used in medical research and diagnosis, has the ability to provide a great deal of information on chemical composition and physical environments[1-3]. MRI has been widely applied in the area of catalysis, dynamics and engineering. However, there has been significantly fewer application of this technique to investigate electrochemical systems. The restrictions of MRI to study electrochemical systems are largely due to experimental difficulties associated with imaging artifacts as a result of the presence of metals commonly found in these systems. However, recent studies[4-7] have shown that MRI has the potential to provide unique chemical and physical information about structural and compositional changes occurring in electrolyte solutions near metal surfaces.

Several electrochemical techniques[8-12] [13] have been used to investigate the process of copper corrosion but to the best of our knowledge very few has the ability to probe spatial distribution and concentration of ions during this process *in situ*.

In this project, artefacts associated with metals in a copper corrosion cell were minimised and the electrochemical processes of copper corrosion were systematically visualised using MRI technique for the first time. This mainly involved the visualization of spatial distribution of ions and concentration during the process of copper corrosion.

To achieve this aim, MRI contrast was produced by differences in magnetic resonance spin-lattice relaxation times (T_1) and spin-spin relaxation times T_2 within pixels from water molecules in the electrolytes solutions.

1.1 Significance of copper corrosion

Copper and its alloys have found wide application in industry and technology due to their availability and economic suitability. They are used as fresh water supply lines and tubing fittings; roofing and architectural uses; industrial and chemical plant process equipment, electrical wiring hard ware's and connectors; marine applications and so on. Copper and its alloys are also ranked among construction materials with high corrosion rate[7,14]. A good understanding of copper corrosion processes would aid in minimising the safety and economic impact of corrosion damages on the numerous copper materials used in industry and technology. For these reasons, there has been much interest in studying the corrosion behaviour of copper under different conditions[7-9,13,15,16].

1.2 Copper corrosion processes

The rate and mechanisms of copper corrosion have been widely studied using different chemical and electrochemical techniques[8,9,11,12,16,17]. The effects of pH, temperature, water chemistry and other additives on the corrosion behaviour of copper have been studied using electrochemical impedance spectroscopy (EIS), electrochemical frequency modulation (EFM), open-circuit potential measurements (OCP), potentiodynamic measurements, potentiostatic measurement and other electrochemical techniques such as cyclic voltammetry[7-9,15,16,18-20]. EIS has been widely used to measure the polarization potential, which gives the rate and mechanisms of copper corrosion under different conditions.

Water chemistry[11,21], temperature and pH[9,22] have been found to have a great impact on the kinetics of pit propagation, and atmospheric corrosion of copper. Scully *et al.*[23] used EIS to

investigate the pit growth of copper in a range of HCO_3^-, SO_4^{2-} and chloride containing waters at different concentrations. They found that water containing high SO_4^{2-} promote high pit growth while those containing chlorides without sulphate ions record slower pit growth. The morphology of the corrosion products was analysed using scanning electron microscopy. The chemistry and composition were investigated using X-ray energy dispersive spectroscopy and Raman spectroscopy respectively[23]. Atacamite, malachite, cuprite and nantokite were identified as the corrosion products.

Scully and Cong using OCP have also studied the effect of chlorine concentration on the natural pitting of copper[10]. They investigated the cathodic reduction reaction kinetics of free chlorine and oxygen on copper microelectrodes. Chlorine reduction was found to be dominant over oxygen reduction[10] and free chlorine was found to increase the cathodic reaction rate and thus raising the OCP towards pitting potentials. EIS has also been used to investigate the rate and mechanisms of atmospheric corrosion of copper in sodium chloride media under different conditions of temperature, pH and chloride concentrations[9,13,24]. It has been found that sodium chloride has a strong effect on copper corrosion particularly in acidic media. The corrosion rate of copper was found to increase rapidly during the initial stage of exposure and then decrease slowly during the last stage of exposure. Most researchers have used X-ray diffraction analysis to analyse the corrosion products obtained as a result of the atmospheric corrosion of copper. Paratacamite, cuprite, atacamite and malachite have been found as the corrosion products during these processes.

The corrosion inhibition of copper under different conditions has also been widely investigated[7,8,14]. The effects of some organic additives were found to markedly reduce the rate of copper and copper alloy corrosion in sodium chloride solutions. Inhibition efficiency was evaluated from weight loss, potentiodynamic polarization, EIS and EFM.

EFM has also been used as a rapid non-destructive technique for corrosion rate measurement. Potentiodynamic and potentiostatic measurements have extensively been used to explain the detailed mechanism of copper corrosion. Other analytical techniques, as ion chromatography and emitted gas analysis have been applied to study the corrosion product obtained from copper corrosion[19,25-27].

While the electrochemical techniques used thus far to investigate copper corrosion have not been able to provide information regarding spatial distribution and concentration of copper ions during these processes, MRI has the potential to provide this information helping in a better understanding of a range of electrochemical corrosion processes. The study of spatial distribution and concentration of copper ions can provide some additional information regarding the rate and mechanism of copper corrosion.

1.3 MRI in electrochemical systems

MRI is one of the few techniques that can provide in-situ characterization of the behavior of electrolyte in electrochemical systems. Most electrochemical techniques provide post-mortem analysis of electrolyte in electrochemical system and techniques like synchrotron analysis can only characterize the electrolyte a few hundreds of microns from the surface. To the best of my knowledge, MRI is the only technique that can provide bulk chemical information and transport measurement in-situ in electrochemical systems. It can allow us monitor corrosion in real-time and will enable us to tinker with the process in future. With this advantage, better understanding of electrochemical corrosion processes, electroplating and other energy devices such as fuel cells and batteries can obtained using MRI.

However, MRI artefacts caused by magnetic susceptibility, eddy current, and radio-frequency shielding due to the presence of metallic materials in electrochemical systems perturb the static magnetic field $\boldsymbol{B}_0$ homogeneity in the MRI spectrometer, and as a result distorted images are obtained. These experimental challenges have severely affected the use of MRI to effectively study electrochemical systems despite it potentials.

To date, there are few examples in literature looking at the study of electrochemical systems using MRI[4-6,28]. Davenport *et al.*[4] used MRI technique to visualise the corrosion of zinc in a Zn/Pt corrosion cell. They constructed a cell comprising of zinc and platinum wire as the working electrodes and concentrated lithium chloride as the electrolyte. The cell was placed inside the magnet of the MRI spectrometer and images within the cell were taken during the galvanic corrosion of the zinc wire. T_1 and T_2 magnetic resonance relaxation times of the electrolyte solution were used to produce contrast for imaging. A time series of T_1 and T_2 maps of the cell were obtained during the corrosion process, as shown in figure 1.1.

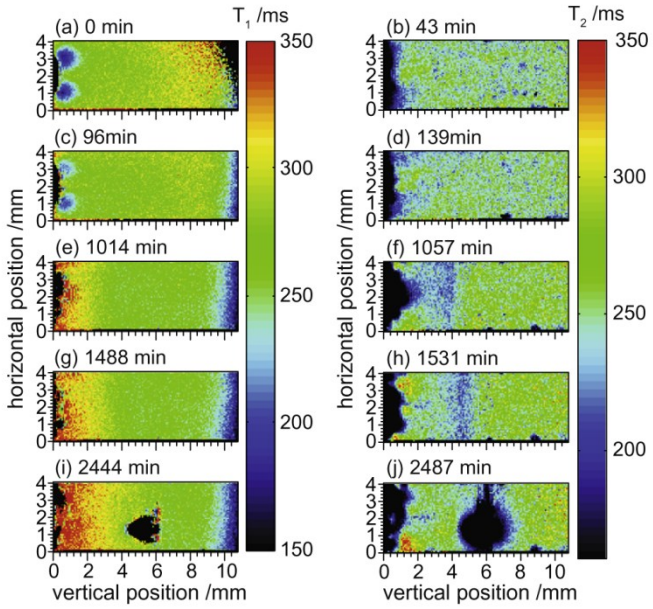

Figure 1.1. A time series of T_1 (a) and T_2 (b) MR images during galvanic corrosion of zinc. The distance scale is measured from the zinc wire. The intervals at which images were collected are shown .Reprinted from ref. 4, copyright (2010), with permission from elsevier.

Variation in the relaxation times of protons in the water molecules of the electrolyte was used to visualise changes in the presence of zinc species. These changes in the zinc species were found to affect the water relaxation times. An initial reduction in T_1 of the electrolyte near the zinc was observed and this was attributed to initial increase in the concentration of zinc ion in the solution. Zinc ion is structure-making ion and so it will coordinate free water molecules and increase their molecular correlation time, which will in turn lead to a decrease in relaxation time. After 17 hours (figure 1.1**e**) there was an increase in T_1, which was related to changes of the zinc species resulting in the formation of some zinc complexes, which are regarded as structure-breaking species[29,30]. In contrast to structure-making ions, structure-breaking ions decrease molecular correlation time and lead to an

increase in the relaxation time. After two days (figures 1.1**i** and **j**) a membranous corrosion product was detected in the MR image, which was reported to have also led to the reduction of the T_2 due reduced mobility and exchange processes.

Some very interesting MRI studies have been recently carried out to visualise changes that occur on battery electrodes and electrolytes. Ohno *et al.*[28] recently constructed a Li-ion battery using as much non-magnetic materials as possible. The cathode and anode were made of $LiMn_2O_4$ coated on aluminium foil and lithium metal respectively and the electrolyte was of $LiClO_4$/propylene carbonate. Relaxation time contrast was used to produce ^{1}H NMR images of the electrolytes near the cathode material during charging of the battery. They found that the paramagnetic cathode material increased the relaxation time of the electrolyte near the cathode (probably due to the presence of Li ion). Grey and co-workers[5] used MR imaging to characterise and visualise non-invasively the formation of microstructures in a Li-ion battery. The electrodes were strips of Li metal soaked in $LiPF_6$/novolyte electrolytes and assembled in an argon-filled glove box. It was shown that orientation of the cell with respect to the rf field has some effect on the quality and appearance of the image. Lithium chemical shift contrast between the bulk-metal and microstructures was used to produce images in two- and three-dimensions, revealing microstructure formation at the negative electrode. Images from the pristine and charged states of the battery were compared and the charged battery revealed a great deal of chemical shift signal at the negative electrode, which was attributed to the microstructure formed after charging the battery. Klett *et al.*[6] used one-dimensional (1D) *in situ* ^{7}Li NMR to visualise build up of concentration gradients in a $LiPF_6$ electrolyte upon application of a constant current through a Li ion battery. Spatially resolved concentration profiles were

also obtained from the cell. The concentration profile was then used to quantify the mass transport properties of the Li-ion battery electrolyte.

Some *in situ* NMR spectroscopic experiment have also been carried out to extract information on the structure and changes that occur in electrochemical systems. The position and shifts of ^{7}Li NMR have been used to extract structural information during cycling of lithium batteries[31]. *In situ* ^{13}C and ^{1}H NMR have also been used to investigate the reaction mechanisms of *p*-benzoquinone electrochemical reduction to hydroquinone[32]. Boron NMR signal from [BF_4^-] has been used to look at the dynamics of the different processes that occur in double layer electrochemical capacitors.

1.4 Structural properties of ions in electrolyte solutions

The MR relaxation times of water molecules in diamagnetic solutions can be explained using the concept of structure-making and structure-breaking ions[29,30,33,34]. Ions that are structure-makers (e.g. Li, Na. fluorides ions and alkaline earth metals) strongly coordinate neighbouring water molecules in the solution and increase the solution viscosity. This will reduce the mobility of water molecules and decrease the relaxation time of the system. Structure-breakers on the other hand, decrease the solution viscosity and increase the mobility of the water molecules. Most of the latter ions are restricted monovalent ions with large sizes (Rb+, Cs+, Br-, NO3- etc). Relaxation time increases as the concentration of these ions increase in solution. Studies on some diamagnetic electrolytes have been used to look at the relationship between concentrations and proton relaxation times. At low concentrations, relaxation rates were experimentally observed to change linearly with concentration. At higher concentrations some researchers also observed the non-linear

dependence of relaxation rates. The different behaviour of structure-maiking and structure-breaking in some diamagnetic salts may be seen in figure 1.2.

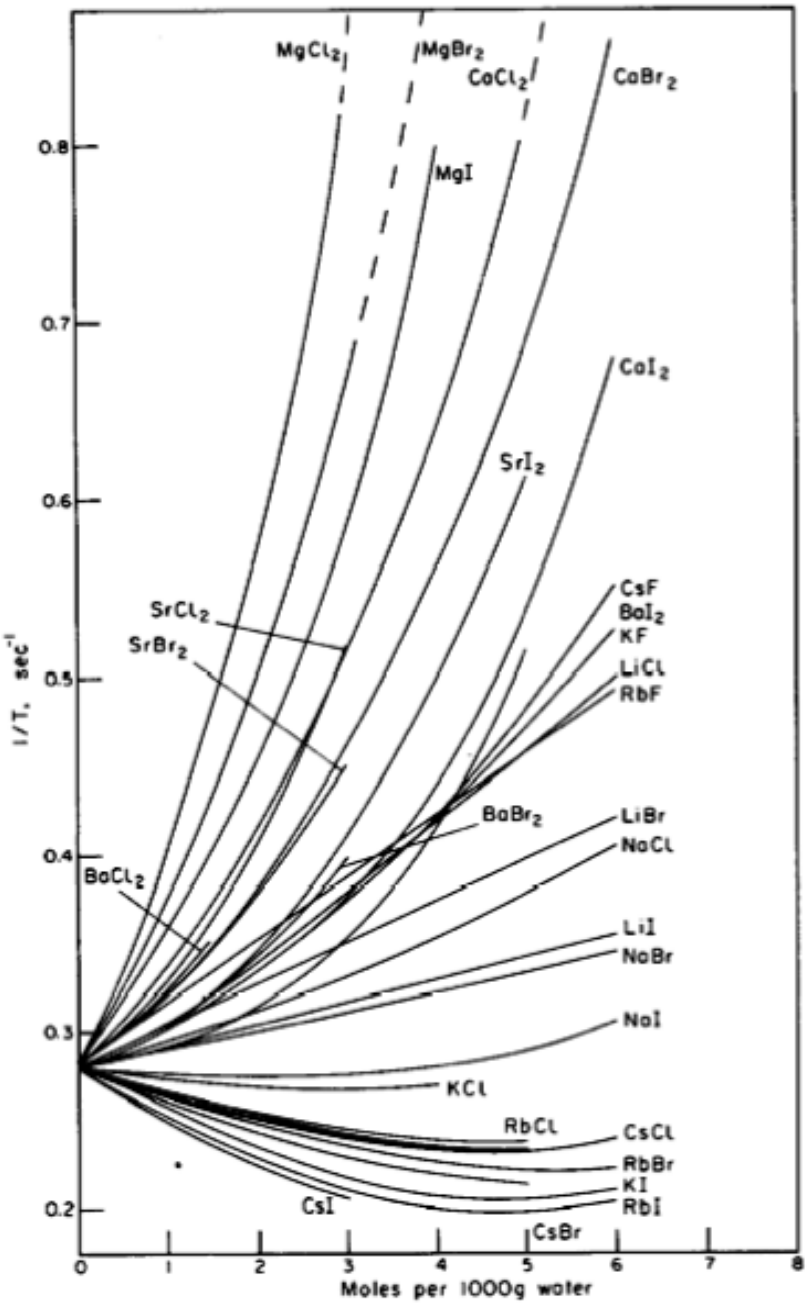

Figure 1.2 Proton relaxation rates of water in aqueous solutions of diamagnetic electrolytes against the electrolyte concentration. Reprinted from ref. 29, copyright (1969), with permission from elsevier.

1.5 Magnetic resonance techniques

A brief overview of the basic theory of NMR and MRI is described in this section. The reader may refer to other excellent textbooks on the subject for more information and deep discussion[35-40].

1.5.1 Basics of NMR

Some nuclei possess spin and the property of this spin is the origin of nuclear magnetic resonance and magnetic resonance imaging[35,36,40] . A nucleus that spins on it axis possesses angular momentum, ρ and charge. The motion of this charged nucleus creates a magnetic moment, μ. The magnetic moment of a nucleus is related to it angular quantum momentum and is described by equation 1.1.

$$\mu = \gamma\rho \qquad (1.1)$$

γ is the gyromagnetic ratio and it describes how strongly magnetic the nucleus is. NMR signal can be obtained when the nucleus under investigation has a net spin value greater than zero. The total nuclear spin of the hydrogen nucleus (^{1}H) with a single unpaired proton is ½. There are many other nuclei with non-zero spin values, but this project considers only the hydrogen nucleus, since it is the only nucleus investigated here.

The ^{1}H nucleus has an angular momentum of I = ½, thus its possesses two degenerate states of (±½). In the presence of an external magnetic field, $\boldsymbol{B}_0$, the nuclear spin states lose their degeneracy. A spin with I = ½ such as a proton is found in one of the non-degenerate spin states designated *spin up* (I = ½) or *spin down* (I = -½). *Spin up* is where

the spins are aligned parallel with the magnetic field and *spin down* where spins are aligned anti-parallel. A torque imposed on the magnetic moment of the nucleus by the magnetic field will cause it to precess (rotate). The nucleus will precess at a frequency (ω) depending on the gyromagnetic ratio (γ) and the strength of the magnetic field $\boldsymbol{B}_0$. The precessional frequency, which is also known as the *Larmor* frequency in angular units of radians s^{-1} or ν in herz, is given by equations 1.2 and 1.3.

$$\omega = \gamma B_0 \tag{1.2}$$

$$\nu = \frac{\gamma B_0}{2\pi} \tag{1.3}$$

The spin states will spread themselves according to the Boltzmann distribution given by equation 1.4.

$$\frac{N_{-1/2}}{N_{1/2}} = e^{-\Delta E / k_b T} \tag{1.4}$$

The populations of *spin up* and *spin down* are denoted by $N_{-\frac{1}{2}}$ and $N_{+\frac{1}{2}}$ respectively. The energy difference between the two states is given by ΔE, k_b is the Boltzmann constant and T is the temperature. There is a slight excess of *spin up* (lower energy) than *spin down* (higher energy). The two possible states *spin up* and *spin down*, in an external magnetic field are shown in the energy level diagram in figure 1.3.

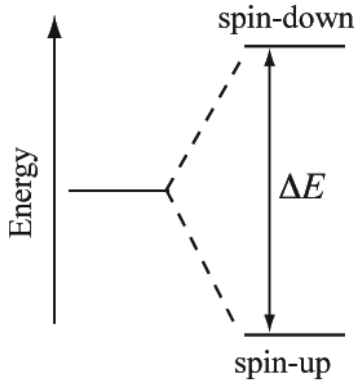

Figure 1.3. Energy level diagram showing "spin up" (parallel orientation) occupying lower energy level and "spin down" (antiparallel orientation) occupying higher energy level.

Summing up the contribution of individual spins for an ensemble of spins produces a macroscopic magnetization vector (M_0). This magnetization vector is aligned in the direction of the external magnetic field ($\boldsymbol{B}_0$). Conventionally, the direction of the magnetic field is defined as the *z*-axis. Application of radio-frequency (rf) pulses at the L*armor* frequency will produce transitions between the *spin up* and *spin down* states; aligning the the magnetization vector onto the transverse *xy* plane. This induces an oscillating voltage in the rf coil, producing the NMR signal. The NMR signal is often refer to as the free induction decay (FID) due to the decay of the amplitude of the induced voltage. The energy of the radio-frequency (rf) radiation must match the energy difference between these two spin states for this transition to occur and it is defined according to equation 1.5.

$$\Delta E = h\nu = \frac{h\gamma B_0}{2\pi} \qquad (1.5)$$

Where h is the Planck's constant.

Relaxation processes lead to transitions between spin states, and eventually the magnetization vector returns to its equilibrium position.

1.5.2 Relaxation processes

Two main relaxation processes characterise the rate of return to equilibrium after the rf excitation pulse. These are known as spin-lattice or longitudinal relaxation (T_1) and spin-spin or transverse relaxation (T_2)[36,40]. T_1 is the process by which the magnetization vector recovers to it equilibrium value, M_0, aligned along the $\boldsymbol{B}_0$ axis. Spins in the neighbouring molecules and ions generate fluctuating local magnetic field. Fluctuations at the L*armor* frequency induce transition between spin states, eventually returning the system to thermal equilibrium. "Through space" interaction between two nuclei or dipolar coupling is the most important contribution to spin-lattice relaxation. The extent of dipolar coupling is very much dependent on the nearness of the two nuclei, and is proportional to $1/r^6$, where r is the distance between the two nuclei. The spin-lattice relaxation is also modulated by the molecular correlation time, τ_c, of the nuclei. The rotational correlation time is the tumbling rate of the nucleus. Shorter correlation times correspond to rapid tumbling. The maximum relaxation rate is achieved when the tumbling rate of the nucleus (τ_c^{-1}) matches its *Larmor* frequency, i.e. $\omega\tau_c = 1$.

Application of a 90^o pulse will equalise the population of *spin up* and *spin down* states and the bulk magnetization vector is moved away from thermal equilibrium (longitudinal magnetization no longer exist), i.e $M_z = 0$. The recovery of magnetization along the z-axis

with respect to time, t, is exponential in behaviour as shown in equation 1.6 and the time constant for this recovery is T_1.

$$M_z = M_0\left(1 - e^{-t/T_1}\right) \qquad (1.6)$$

Apart from rotating the equilibrium magnetization to the xy axis, through a 90^o excitation pulse individual spins are also aligned along the transverse plane. Spins will initially have phase coherence, i.e they will precess synchronously. However, this phase coherence can only be maintained if the magnetic field experience by each spin in the system is exactly the same. Phase coherence is gradually lost as a result of molecular interactions as some spins advance while others lag behind on their precessional path, leading to fanning-out of macroscopic magnetization vector in the transverse plane. This decay process is exponential with time, t, as shown in equation 1.7, where M_0 is the initial transverse magnetization at $t = 0$.

$$M_{x/y} = M_0 \ell^{-t/T_2} \qquad (1.7)$$

The time constant for spin-spin (transverse) relaxation is referred to as T_2 and is related to the intrinsic properties of the spins system. Inhomogeneities in the external magnetic field can also affect spin-spin relaxation. The time constant $T_2(\Delta B_0)$ is associated with these

inhomogeneities. The two combined relaxation time constants contribute to the observed decay of transverse magnetization designated T_2* given by equation 1.8.

$$\frac{1}{T_2^*} = \frac{1}{T_2} + \frac{1}{T_{2(\Delta B_0)}} \qquad (1.8)$$

1.5.2.1 T_1 measurement – inversion recovery

The T_1 relaxation is usually measured using a pulse sequence as shown in the schematic diagram in figure 1.4.

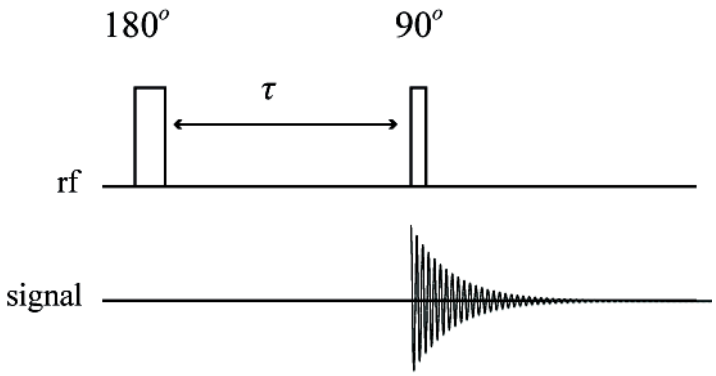

Figure1. 4. Schematic representation of an inversion recovery pulse sequence for a T_1 relaxation measurement.

This method requires the use of an initial 180° rf pulse to flip the equilibrium magnetization vector onto the –*z* axis[36]. However, magnetization along the negative *x*-axis cannot be measured. As the magnetization begins to return to its equilibrium position

through a suitable time delay τ, a second $90^{o}x$ pulse is used to rotate the *z*-magnetization onto the transverse *xy* plane where the signal can be detected. The signal intensities depend on the length of the delay time τ. The whole process is repeated for different values of τ in order to map out the recovery of the inverted magnetization and to produce series of spectra with various intensities. By plotting these intensities against τ, a smooth exponential curve is obtained (figure 1.5) which can be fitted to equation 1.9 to extract T_1.

$$M_Z = M_0(1 - 2e^{-\tau/T_1}) \qquad (1.9)$$

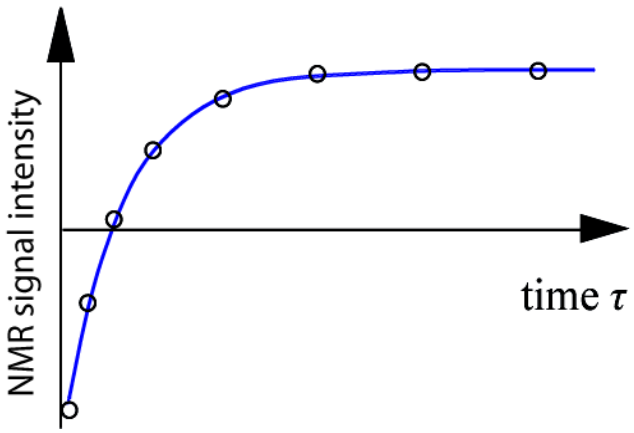

Figure 1.5. Inversion recovery (exponential) curve fitted to equation 1.9 to extract T_1, the longitudinal time constant.

1.5.2.2 T_2 measurement – Carr-Purcel-Meiboom-Gill (CPMG)

Carr-Purcel-Meiboom-Gill, CPMG is a pulse sequence used to measure T_2 relaxation[35,36,38]. It involves the initial use of a 90° excitation pulse to align the magnetization onto the transverse *xy* plane. At the beginning, all the precessing nuclei spins have phase coherence, but T_2 relaxation acts to de-phase the spins, with some spins moving slower and some moving faster than the L*armor* frequency. The first 90° pulse is followed by a time delay τ, a 180° excitation pulse which will rotate the spins about the transverse plane. Now, the spins will begin to re-phase, and after a second delay of τ, phase coherence is restored and a Hahn-echo (spin-echo) is formed. The interval between the initial 90° excitation pulse and the top of the echo is called the echo time. Figure 1.6 shows a schematic diagram of a Hahn-echo pulse sequence.

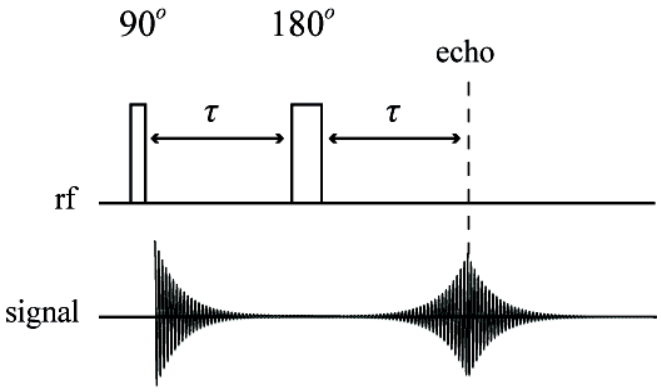

Figure 1.6. Schematic representation of a Hahn-echo pulse sequence.

If spins diffuse to a region where there is different $\boldsymbol{B}_0$ field, the 180° pulse does not completely re-phase them. The CPMG experiment consists in a series of τ-180-τ, where τ is typically in hundreds of milliseconds. T_2 of the sample can be calculated by plotting the intensities resulting from these echoes against time (figure 1.8) and fitting into equation 1.7. The pulse sequence for CPMG is shown in the schematic diagram in figure 1.7.

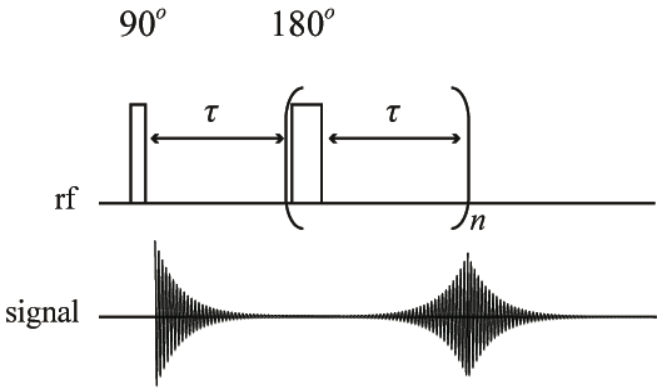

Figure1. 7 A schematic diagram of a CPMG pulse sequence for a T_2, relaxation time measurement.

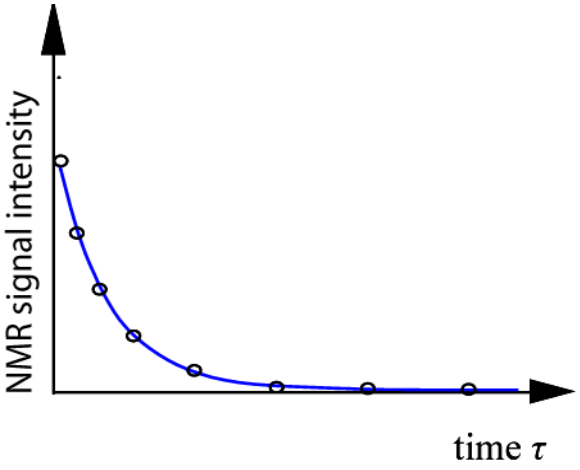

Figure 1. 8. CPMG (exponential) curve fitted to equation 1.7 to extract T_2, the transverse relaxation time constant.

1.5.3 Magnetic resonance imaging

Magnetic resonance imaging MRI techniques uses magnetic field gradients to spatially locate the positions of nuclei in a sample. Using MRI, one-, two, and three-dimensional images of opaque and non-opaque systems can be acquired non-invasively. MRI method is very versatile and has numerous applications.

1.5.3.1 Basics of MRI

In magnetic resonance imaging, magnetic field gradients are applied linearly in the direction of $\boldsymbol{B}_{0,}$ the magnetic field gradients in the *x*, *y*, and *z* direction, where the $\boldsymbol{B}_0$ field is in the *z* direction are defined by equations 1.10, 1.11, 1.112 respectively:

$$G_z = \frac{dB_z}{dx} \qquad (1.10)$$

$$G_y = \frac{dB_z}{dy} \qquad (1.11)$$

$$G_z = \frac{dB_z}{dz} \qquad (1.12)$$

By modifying equation 1.3 to include contribution from the magnetic field gradients, the precessional frequencies of nuclei are then defined as, equation 1.13[35]:

$$\omega(r) = \gamma(B_0 + G\mathbf{r}) \qquad (1.13)$$

Where $\boldsymbol{G}$ in equation 1.4 is the magnetic field gradient and ω (r) is the resonance frequency at position **r**.

The effect of applying magnetic field gradients along the *x*-direction is shown in figure 1.9. The $\boldsymbol{B}_z$ magnetic field is not influenced in the absence of magnetic field gradients. By applying the gradients, the $\boldsymbol{B}_z$ magnetic fields will no longer be homogenous and will vary with position along the *x*-axis.

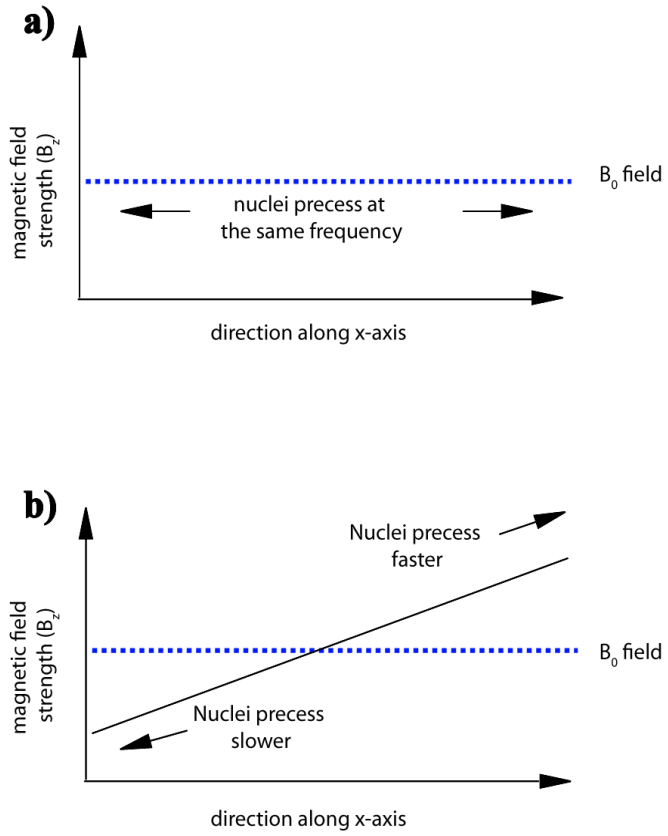

Figure 1.9 a) Variation of the B_z magnetic field with position along the x-axis. b) Variation of the B_Z magnetic field when a linear magnetic field gradient is applied in the x-direction.

1.5.3.2 Frequency encoding

The precessional frequencies of nuclei in a sample become position dependent by the application of magnetic field gradients. This assertion forms the basis of frequency encoding. In frequency encoding, a constant magnetic field gradient is applied during the process of signal acquisition along a direction. This gradient generates magnetic field that increases in strength from right to left. The corresponding changes in the L*armor*

frequencies make spins on the left side precess slower than the ones on the right side. Fourier transforming this acquired signal results in a frequency domain spectrum. The signal intensity is then proportional to the number of nuclei with a particular position along the frequency encoding gradients. For one-dimensional imaging experiment, the resultant spectrum is a one-dimensional profile of all the spins in the *y*- and *z*- axes projected onto the *x*-axis, figure 1.10.

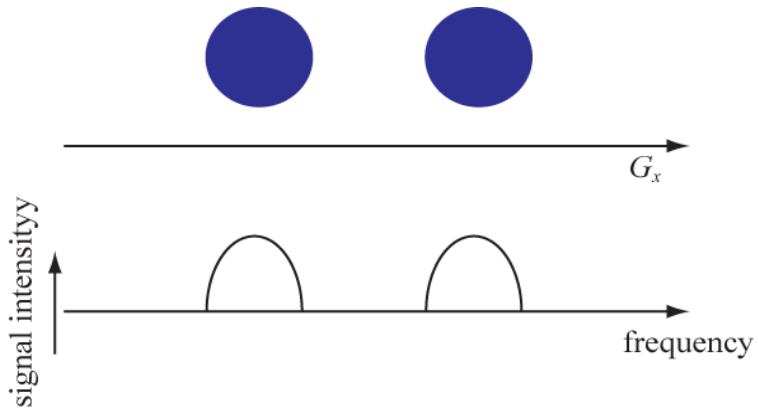

Figure 1.10. One dimensional frequency encoding spin density profile of two tubes of water acquired with gradients applied along x-axis

1.5.3.3 Phase encoding

In phase encoding, a magnetic field gradient from top to bottom in the *y* direction is switched on for a fixed time interval but switched off prior to the signal acquisition. Such phase encoding gradient alters the *Larmor* frequencies of nuclei according to their position along the gradient. As the gradient is switched off prior to signal acquisition, nuclei will

again precess at the same frequency. The result is a phase shift of the spins relative to each other (a helix of phase is wound), figure 1.11. The strength of the gradient applied and the duration for which it is applied for determines the pitch of the helix. The wavelength of the helix is the distance over which a 360^{o} phase shift occurs and is denoted by λ. Phase encoding needs multiple excitations with increasing gradients strengths. Spatial information in the phase encoding direction is encoded in the value of the phase shift.

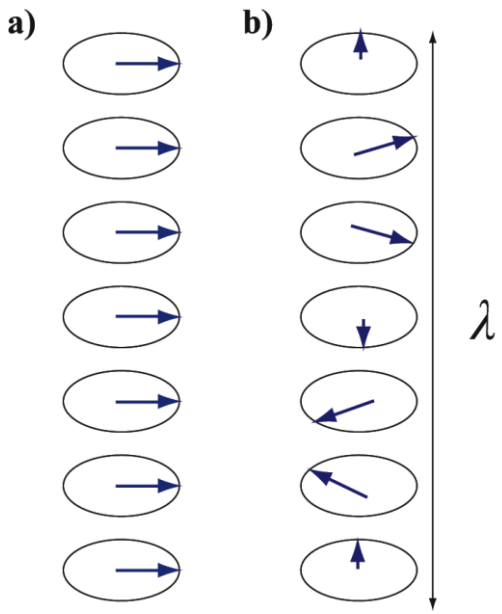

Figure 1.11 a) Phase spin packets following a 90^{o} pulse without the application of magnetic field gradients. b) Phase spin packets after the application of linear magnetic field gradients winding a helix of phase. The wavelength of the helix of phase is given by λ.

1.5.3.4 Slice selection

Slice selection is the excitation of proton nuclei within a chosen slice (vertical or horizontal) through a sample by the simultaneous application of a magnetic field gradient and an rf pulse with a frequency equal to their L*armor* frequency (frequency selective soft rf pulse)[35,38]. The duration of the rf pulse can be used to control the bandwidth of the excited frequencies. Application of an rf pulse that matches the Larmor frequency of the desired slice will only excite protons nuclei within the chosen slice while the rest of the sample remains unaffected. The strength of the gradients applied can define the slice thickness. An rf pulse of a given frequency bandwidth produces a thin slice if the gradient is strong and a thick slice if the gradient is weak.

1.5.3.5 *k*-space

A combination of frequency and phase encoding gradients in an imaging experiment is used to build up an array of NMR data over reciprocal space known as ***k***-space. ***k***-space is a mathematical area that is used to store NMR data. It is defined by the ***k***-space vectors $\boldsymbol{k}_x$, $\boldsymbol{k}_y$, and for 3D images k_z. For 2D imaging, ***k***-space has two axes with the horizontal axis ($\boldsymbol{k}_x$) representing the frequency information and the vertical axis ($\boldsymbol{k}_y$) the phase information (***k***-space raster) as shown in figure 1.13. The data acquired from NMR signal are sampled for each point in the ***k***-space raster. 2-D Fourier transformation results in the reconstruction of an MR image. The data in ***k***-space here is Fourier transformed to real space which gives the image. The line in ***k***-space do not correspond one to one with the line in the resulting image. Rather, data in the centre of ***k***-space primarily determines contrast in the image while the periphery primarily contains spatial information.

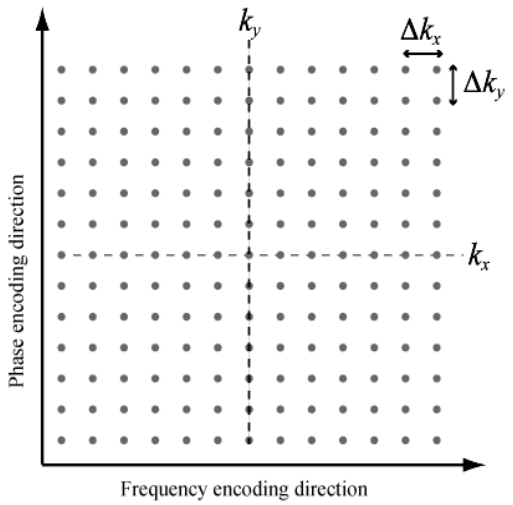

*Figure 1.13. A two-dimensional sampling of a **k**-space raster, showing a combination of gradients in a frequency encoded x-direction and a phase encoded y-direction.*

The horizontal axis $\boldsymbol{k}_x$ is traversed in time by applying a frequency encoding gradient. In the *x*-direction, the ***k***-space sampling interval Δk_x, is given by equation 1.14, where Δt is the sampling interval of the FID and G_x is the read gradient.

$$\Delta k_x = \frac{\gamma G_x \Delta t}{2\pi} \qquad (1.14)$$

In order to collect the entire ***k***-space data, it is essential to use negative read precursor gradient. The vertical axis $\boldsymbol{k}_y$ is traversed through the application of a series of phase encoding gradients of varying strengths. In this axis, the ***k***-space sampling interval Δk_y is

given by equation 1.15, where ΔG_y are the phase encoding gradients step size and t is the duration of the phase encoding gradients.

$$\Delta k_y = \frac{\gamma \Delta G_y t}{2\pi} \tag{1.15}$$

Positive values of $\boldsymbol{k}_y$ involve positive phase encoding gradients while negative $\boldsymbol{k}_y$ is accessed using negative gradients. Each horizontal line in the raster is acquired using a single excitation and read out during signal acquisition[35].

1.5.3.6 Image resolution and field of view

The size of spatial features that can be distinguished in an image is determined by the image resolution. A higher resolution permits smaller features to be resolved. The maximum spatial distance that can be displayed in an image is referred to as the field of view (FOV). If the sample being imaged extend outside the FOV or the FOV is chosen wrongly, image aliasing can occur. The locations of spins outside the FOV are wrongly located, resulting in image "fold-over". In imaging experiments, spatial resolution is determined by the ***k***-space sampling intervals and the number of points in the raster, i.e how far out the data is sampled into k-space. Equation 1.16 and 1.17 give the spatial resolution in the frequency and phase encoding directions respectively. Where n_x and n_y are the number of data points in the k_x and k_y directions respectively

$$\frac{1}{\Delta x} = n_x \Delta k_x \tag{1.16}$$

$$\frac{1}{\Delta y} = n_y \Delta k_y \tag{1.17}$$

In the frequency encoding direction, the limit to spatial resolution is related to the line width, $\Delta\nu$ of the NMR signal being acquired as given by equation 1.18.

$$\frac{1}{\Delta x} = \frac{\gamma G_x}{2\pi\Delta\nu} \tag{1.18}$$

The FOV in the frequency and phase encoding directions has an inverse relationship with the respective ***k***-space sampling interval, equation 1.19 and 1.20.

$$x_{\max} = \frac{1}{\Delta k_x} \tag{1.19}$$

$$y_{\max} = \frac{1}{\Delta k_y} \tag{1.20}$$

1.5.3.7 Contrast in MRI

Distinguishing between different regions of chemical composition and/or physical environment is very important in MR imaging. Image contrast can be achieved by making the signal intensity of the pixels within an image reliant upon NMR parameters of the nuclei contributing to them. There are several ways of making contrast within an image but only two of these methods would be briefly explained here.

1.5.3.7.1 Spin density

Spin or proton density is the number of excitable spins per unit volume (pixel) and the signal intensity in an image is exclusively determined by the number of these spins in that pixel. Proton density can be accentuated by minimizing other parameters such T_1 and T_2 relaxation times in the system. Such images are termed spin density or proton density images.

1.5.3.7.2 T_1 and T_2 relaxation contrast

Images with contrast that is mainly determined by T_1 and T_2 are called T_1- and T_2-weighted images. Here the signal intensity is chiefly affected by the T_1 or T_2 relaxation times of the nuclei, although, the signal intensity is also determined partly by the spin density. This is important if components in the sample have different T_1 and/or T_2 relaxation times. T_1-weighted image is produced if the repetition time T_R is shortened so that it is comparable to the longest T_1 present in the sample ($T_R > 5 \times T_1$). Regions with shorter T_1 will have high

signal intensities because the T_1 relaxation effects are negligible. However, regions with longer T_1 relaxation times will give abridged signal as a result of partial relaxation between repetitions. On the other hand, if the repetition time is kept sufficiently long and the echo time, T_E is extended comparable to T_2 of the sample, T_2 weighted image is obtained. The regions containing nuclei with shorter T_2 will give reduced intensity due to de-phasing compared to regions with longer T_2.

1.6 RARE imaging

Rapid acquisition with relaxation enhancement (RARE) is a pulse sequence that is designed to reduce imaging time[41]. It is based on a spin echo imaging sequence. In this sequence, spins are refocused and a spin echo is obtained several times, n, per excitation. A multiple line of $\boldsymbol{k}$-space is then collected for single excitation thereby reducing the experimental time. The number of echoes obtained for each excitation is called RARE factor. As the RARE factor increases, the experimental time decreases. The smaller imaging time is normally achieved at the detriment of the signal-to-noise ratio.

1.7 Metal artefacts in MRI

Any feature appearing in an image, which is not present in the object being imaged is refered to as image artefact[35]. Artefacts may arise due to the properties of the material being imaged, improper operation of the imager or as a result of faults in the imaging equipment. Image artefacts are classified according to their sources namely, magnetic susceptibility artefacts, radiofrequency artefacts, chemical shift artefacts, motion and flow artefact and aliasing[35,42]. In this section, we are going to be concerned mainly with artefacts

that are produced as a result of the presence of metallic materials. The presence of metals in systems being imaged can significantly impede imaging for several reasons. First of all, no MRI signal can be obtained from the metal, making the region where the metal is on the MR images appearing dark. Also, the presence of metal can result in severe variations in the static magnetic field due to susceptibility differences between metal and surrounding water protons or tissues. The two main sources of metal-induced artefacts are magnetic susceptibility and radiofrequency (rf) artefacts[43,44].

1.7.1 Magnetic susceptibility artefacts

Magnetic susceptibility is the ability of a material to be magnetised on exposure to an external magnetic field[39,43]. Different materials have different magnetic susceptibilities. Those with positive values of magnetic susceptibility are called paramagnetic materials, while those with negative values are called diamagnetic materials. Metallic materials generally have high magnetic susceptibility and when they are placed in magnetic field, they develop magnetic moments and distort the applied field[43]. A variety of artefacts in MRI arise when materials with large magnetic susceptibility differences are brought together near an imaging plane, resulting in long-range magnetic field perturbations. Susceptibility differences can arise at interfaces between solid-liquid, liquid-air or liquid-liquid. The presence of metals can result in severe variations in the static magnetic field $\boldsymbol{B}_0$ due to magnetic susceptibility differences between metal and surrounding environment (e.g water molecules or tissue)[42,43,45-47]. Differences in magnetic field can cause large resonance frequency variations, resulting in a variety of artefacts in MRI. Inhomogeneity in the static field can be as a result of internal magnetic field gradients, which are produced by the material susceptibility effects, which in turn will cause mis-registration of the position of

spins. The main artefacts that arise in imaging are signal loss due to de-phasing, displacement artefacts, and failure of fat suppression in medical MRI[48]. In imaging near metal object, the magnetic field variations can be very rapid resulting in the magnetization within a voxel to precess at a very high rate. This gives rise to lose of coherence or de-phasing and signal loss. In images, this appears as a black area where signal was espected. De-phasing artefacts can be prevented by the use of spin-echo imaging technique[48]. Interferences with the read and slice encoding gradients give rise to displacement artefacts resulting in signal loss and signal pile up[48]. The magnitude of the susceptibility artefacts depend on the susceptibility of the metal and other parameters, including the magnetic field strength, geometry of the metal, scan sequences used, the imaging band width and the orientation of the metal with respect to the $\boldsymbol{B}_0$ magnetic field and the read and phase encoding gradients[43,48].

Generally, susceptibility artefacts can be minimised using spin echo sequences. This is because the 180^{o} refocusing rf pulse corrects for T_2^{*} effects and spin echo sequences themselves are fairly insensitive to static field inhomogenieties. Other imaging methods used to minimise susceptibility artefacts from metal implants in medical imaging are; use of spin echo and fast spin echo sequences instead of gradients echo sequences, swapping of the phase- and frequency-encoding axes, imaging with a wider receiver bandwidth, aligning the longitudinal axis of the metal implants with the axis of the external magnetic field and the using of short T_1 inversion recovery rather than frequency-selective fat suppression technique.

1.7.2 Radiofrequency artefacts

Radiofrequency artefacts can arise due to the presence of conducting metallic materials in an imaging plane[44,49,50]. The electromagnetic rf pulses applied for excitation or refocusing purposes can be influenced by the presence of metals with high electrical conductivity, causing them to induce current known as eddy current in the metals[49,51-53]. The induced electrical current emanates from the time varying magnetic field component $\boldsymbol{B}_1$ of the rf waves as described by Faraday's, law of induction. The correlated electric field $\boldsymbol{E}_1$ can also cause direct acceleration of electrons in the metals. Consequently, the uniformity of the $\boldsymbol{B}_1$ exciting field is perturbed, resulting in either a lower or higher amplitude of $\boldsymbol{B}_1$ near the metal part, which correspond to a lower or higher effective excitation angle respectively. The eddy current generated in the conducting materials by the high-frequency rf pulses would create magnetic counter fields, thereby changing the effective rf pulses amplitude across the imaging region. This would modify the spin-echo signal and affects the image reconstruction. These variations in excitation angle can cause considerable artefacts. The magnitude of rf artefacts depend on the orientation and arrangement of the metallic part in the spectrometer with respect to the rf field.

1.8 Paramagnetic contrast agents

Paramagnetic substances are usually used to enhance relaxation time contrast in MR images[54,55]. These are substances (e.g dissolved metal ions) that contain unpaired electrons in their outer electron shell or in their atomic nuclei. The presence of unpaired electrons in paramagnetic substances brings about localised magnetic field fluctuations that enhance the relaxation rate of solvent nuclei in their vicinity. These substances are commonly called contrast agents. A number of different paramagnetic metals ions that can give contrast

enhancement, including Cu^{2+}, Mn^{2+}, Mn^{3+}, Fe^{3+} and Gd^{3+}. The magnitude with which the contrast agent enhances the relaxation rate is termed relaxivity and usually expressed in units of mM^{-1} s^{-1}. The effect of paramagnetic species on T_1 is generally found to be more pronounced than that on T_2[54].

1.8.1 Relaxivity

Paramagnetic substances increase T_1 and T_2 relaxation rates of solvent nuclei. The contribution from paramagnetic and diamagnetic species to the relaxation rate are additive to such solution and can be described by equation 1.21[54]. In this equation, $(1/T\text{i})_o$ refers to the observed relaxation rate of solvent in the presence of paramagnetic species, $(1/T_i)_d$ refers to the diamagnetic solvent relaxation rate in the absence of paramagnetic species, and $(1/T_i)_p$ is the additional paramagnetic contribution.

$$\left(1/T_i\right)_o = \left(1/T_i\right)_d + \left(1/T_i\right)_p \qquad (1.21)$$

The relaxation rate of the solution in the absence of solute-solute interaction is linearly dependent on the concentration of paramagnetic species ([C]) in units of mM^{-1} s^{-1}. The relaxivity r_i refers to the slope of the dependence in this units, equation 1.22[54,56].

$$\left(1/T_i\right)_o = \left(1/T_i\right)_d + r_i[C] \qquad (1.22)$$

The interactions that bring about the relaxivities of water protons are broadly classified into two mechanisms namely, inner-sphere relaxation mechanism and outer-sphere relaxation mechanism[54,57-59]. The relaxation of a water proton that is bound directly to the primary co-ordination sphere of the paramagnetic metal ion is called inner-sphere relaxation mechanism[54,57-59]. On the other hand, outer-sphere relaxation mechanism involves the enhancement of relaxation processes where water protons are not directly bound to the contrast agent.

1.8.1.1 Inner-sphere relaxation

Equation 1.23 describes the inner-sphere contribution to relaxivity for T_1[54,58]. P_M and q in the equation are the mole fraction of metal ion and the number of water molecules bound per metal ion respectively. T_{1M} is the relaxation time of the co-ordinated water, and τ_M is the residence life time of the bound water protons.

$$\frac{1}{T_1} = \frac{P_M q}{T_{1M} + \tau_M} \qquad (1.23)$$

The value of T_{1M} is governed by the molecular correlation time, τ_R, whereby slowly tumbling paramagnetic contrast agents leads to faster relaxation rate, and hence relaxivity. If numerous coordination sites are accessible (higher number of bound water molecules, q) and bound water protons are in fast exchange with the bulk solvent (short residence time, τ_M), then the effects of the paramagnetic contrast agent will be greater, (higher relaxivity).

The mobility of metals ions coordinated to large chelates or macro-molecules can be reduced greatly. Complexation of these metal ions will increase their molecular correlation time, and hence relaxivity.

1.8.1.2 Outer-sphere relaxation

Outer-sphere relaxation can take two forms second relaxation and true outer-sphere relaxation mechanisms[54,58]. Outer sphere relaxation where water molecules are hydrogen bonded into the second co-ordination sphere is relaxed through dipolar mechanisms. Second-sphere relaxation has similar mechanisms to inner-sphere relaxation, and is controlled by analogous parameters. True outer sphere relaxation is brought about as a result of diffusion of water molecules near to the paramagnetic metal-ion. The relaxivity is focused on the electronic relaxation time of the metal, the distance of the closest approach of solvent and solute, *d,* and the sum of their diffusion coefficients as described by equation 1.22, where τ_D is the translational diffusion time, and D_s and D_1 are the diffusion coefficients of the metal-ion and water molecules respectively.

$$\tau_D = \frac{d^2}{3(D_1 + D_s)} \qquad (1.24)$$

1.9 X-ray diffraction analysis

X-ray diffraction analysis has been widely used for the identification and structural elucidation of crystal substances. A brief description of the basic theory of this technique is given here. The reader is referred to some excellent text for a more in depth discussion of the technique[60,61]. X-ray interacts with electrons in matter and a beam of X-rays impinging on an inorganic material will be scattered in various directions by the atomic electrons. If distances comparable to the wavelength of the X-rays separate the scattering centres then interference between the X-rays scattered from particular electron centre can occur. For an ordered array of scattering centres this can give rise to interferences maxima and minima. A study of X-rays scattered by crystalline solid provides a wealth of structural information. X-ray powder diffraction technique serves as one of the most reliable methods for the identification of crystalline materials. X-rays perforating below the surface of a crystalline materials are scattered by the individual parallel layers of atoms; each atomic layer as a new although weak source of X-rays. To be reinforced in a given direction at an angle of θ, the spacing, *d,* between crystal planes must be rigorously related to the wavelength of the x-ray radiation. At a given angle, X-ray of one definite wavelength will be constructively reinforced and the variation are related by Bragg's law, $\lambda n = 2d \sin\theta$ where n is the order of diffraction. The diffraction method could be carried out on either a single crystal or on a powder sample. The diffracted X-rays may be recorded either photographically or by means of counting device such as scintillating counter. Powder samples normally contain many crystals (crystallites) arranged at random angles and the combined effects of all their various crystal planes is to produce a series of cones of scattered X-rays. In order to obtain powder X-ray diffraction data in a form useful for analysis, the positions of the various diffraction cones need to be determined. This may be

achieved by using a rotating detector. The readout is a series of peaks, the heights and areas of which are proportional to the intensity of the lines and position are in terms of 2θ degree. The angles may be readily translated into *d*-values where the wavelength of the incident radiation is known. X-ray powder diffraction technique is often used as a "fingerprint" method. It involves comparing the X-ray powder diffraction pattern of the sample under test with database by the joint committee on powder diffraction standards (JCPDS). The powder pattern is usually sufficient to characterise the compound under test and also provides information on the number of phases present in the compound.

In the next (experimental section), horizontal and vertical spin density images of the copper cell with the copper strip position at different orientations with respect to the rf field would be taken. This is to get the best orientation the cell needs to be MRI spectrometer in order to minimise artefacts and obtain a distortionless images as the copper strip corrodes. T_1 and T_2 maps and optical images of the copper cell at regular intervals would then be taken to show the distribution of copper ions and concentration during copper corrosion process over time. Relaxations measurements of varying $CuSO_4$ solutions in sodium chloride/agar gel would be carried out as the control measurement to show the dependence of magnetic resonance relaxation times with varying copper concentrations. X-ray diffraction analysis of the final corrosion product would also be carried out to identified the resulting substances from the corrosion process.

2 Experimental

2.1 Solution preparation

Copper sulphate (98%), sodium chloride (99%), and agar were purchased from Sigma-Aldrich and were used as supplied. Stock solution, of copper sulphate was prepared by dissolving the appropriate amount of the salt in distilled de-ionised water. A concentration range between 1 mM to 10 mM of copper sulphate was prepared from the stock solution. The concentration of sodium chloride used in the cell was 0.5 M. Sodium chloride/agar electrolyte was prepared by bringing 10 mL 0.5 M sodium chloride solution to boil, and adding 0.15g agar (1.5 % w/v) slowly while the solution was stirred. The gel was then allowed to cool. Control samples were made from various solutions of copper sulphate (0 mM, 1mM, 2 mM, 5 mM amd 10 mM) in 0.5 M sodium chloride and 1.5 % w/v agar. The control sample solutions were made in glass vials of 12 mm × 80 mm dimension.

2.2 Copper corrosion cell

A schematic diagram of the copper cell used inside the spectrometer magnet is shown in Figure 2.1. The electrolyte was 0.5 M sodium chloride in 1.5 % w/v agar. A copper strip (Advent, 99.55 %, 0.25 mm thickness) was embedded in agar/sodium gel, contained in the glass vial.

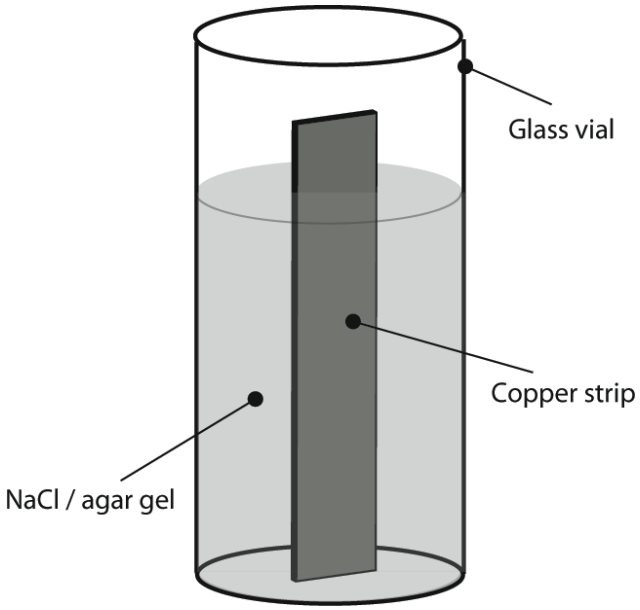

Figure 2.1. Corrosion cell schematic diagram.

2.2 T_1 and T_2 relaxation time experiments

A Bruker DMX300 spectrometer equipped with a vertical bore superconducting magnet (7 T) operating at ^{1}H resonance frequency of 300 MHz was used for relaxation time and imaging experiments. All relaxation time experiments were performed at a temperature of 20 ± 0.2 ^{o}C, in a 25 mm radiofrequency coil.

T_1 and T_2 relaxation times were measured for 0 mM, 1 mM, 2 mM, 5 mM and 10 mM copper sulphate solutions in 0.5 M sodium chloride gel and 1.5 % w/v agar (control samples solutions). T_1 relaxation times were measured for all the control samples using an inversion recovery experiment (180^o -τ -90^o). For each sample solution, 33 acquisitions were collected with variable delays (inversion recovery) ranging from 2.5×10^{-3} s to 15 s. T_2 relaxation times were obtained by Carr-Purcell-Meiboom-Gill (CPMG) experiments.

For all the control sample solutions, 16 experiments were performed, where the echoes times ranged from 1 s to 1024 ms.

The spectral width for both inversion recovery and CPMG experiments was 10 kHz. 16k data points and four signal averages were acquired. The durations of the hard rf pulse were of 45 ms for the 90^{o} rf pulse and and 90 ms for the 180^{o} rf pulse. Prospa and kaleidagraph softwares were used to analyse the set of data obtained from both T_1 and T_2 experiments.

Two-dimensional data sets of spectral data against time were produced from the variable delay (inversion recovery) or variable counter (CPMG) list. The signal intensity against time for the inversion recovery experiment was fitted to a single-exponential recovery function to extract the T_1 value (equation 1.9). The signal intensity against time for the CPMG was fitted to a single-single exponential decay to extract T_2 value (equation 1.7).

2.3 MRI experiments

PARAVISION was used to acquire the data for the spin density and T_1 and T_1 weighted imaging experiments. RARE fast (32 rare factor) imaging technique was used to acquire all the images. Horizontal spin density images and T_1 and T_2 maps of the copper corrosion cell were acquired with a slice thickness of 1 mm, a field of view of 20 mm × 20 mm and a matrix dimension of 128 (phase) 128 (read) pixels, resulting in a pixel size of 0.156 mm × 0.156 mm. Vertical spin density images, T_1 and T_2 maps of the cell and control samples maps were acquired with a slice thickness of 1 mm, a field of view of 40 mm × 20 mm and a matrix dimension of 128 (read) × 64 (phase), resulting in a pixel size of 0.313 mm × 0.313 mm. The vertical images were acquired by taking a vertical slice through the cell (as shown with grey dotted lines in figure 3.1**a-f**). A repetition time of 15000 ms was used

(>5T_1) for the T_1 and T_2 maps of the cell and the T_1 and T_2 maps of the cell taken at different orientations with respect to the rf field. For the spin density images, a repetition time of 1000 ms was used. Sixteen, four and two signal averages were collected for the T_1 and T_2 maps of the cell, T_1 and T_2 maps of the cell taken at different orientations with respect to the rf field, and the spin density images respectively. T_1 relaxation and control maps were obtained from a series of eight spin echo images (MR) with inversion recovery delays, ranging from 5.88 to 5000 ms, all with an echo time of 3.45 ms. T_2 relaxation and control maps were obtained by acquiring eight images and varying the echo time from a minimum value of 52 ms to a maximum value of 758.5 ms. The cell was positioned in the MRI spectrometer in such a way that the copper strip is aligned parallel to the direction of the rf field. T_1 and T_2 maps were collected at regular interval of three days over a period of 11 days.

2.3.1 Optical measurement

A Cannon power shot A550 digital CCD camera was used to acquire optical images of the copper corrosion cell over a period of 11 days.

2.3.2 X-ray diffraction analysis

After eight weeks, the gel electrolyte samples from the copper corrosion cell were extracted and air-dried in the laboratory. The dried products were then finely grounded. The corrosion products were analysed on a D8 AVANCE diffractometer using CuKα (wavelength, 1.54060 Å), setting generator to 40KW, 30 mA with a step size of 0.02^o. Time /step is 58.1 seconds with a total scan time of 30 minutes at 2θ value ranging from 50 to 80 Degrees.

3 Results and Discussion

3.1 Spin density images and maps of the copper cell

Horizontal and vertical spin density images of the copper cell taken at different orientations with respect to the rf field are shown in figure 3.1. Horizontal T_1 and T_2 maps with the cell positioned at different orientations with respect to the rf field are shown in figure 3.2.

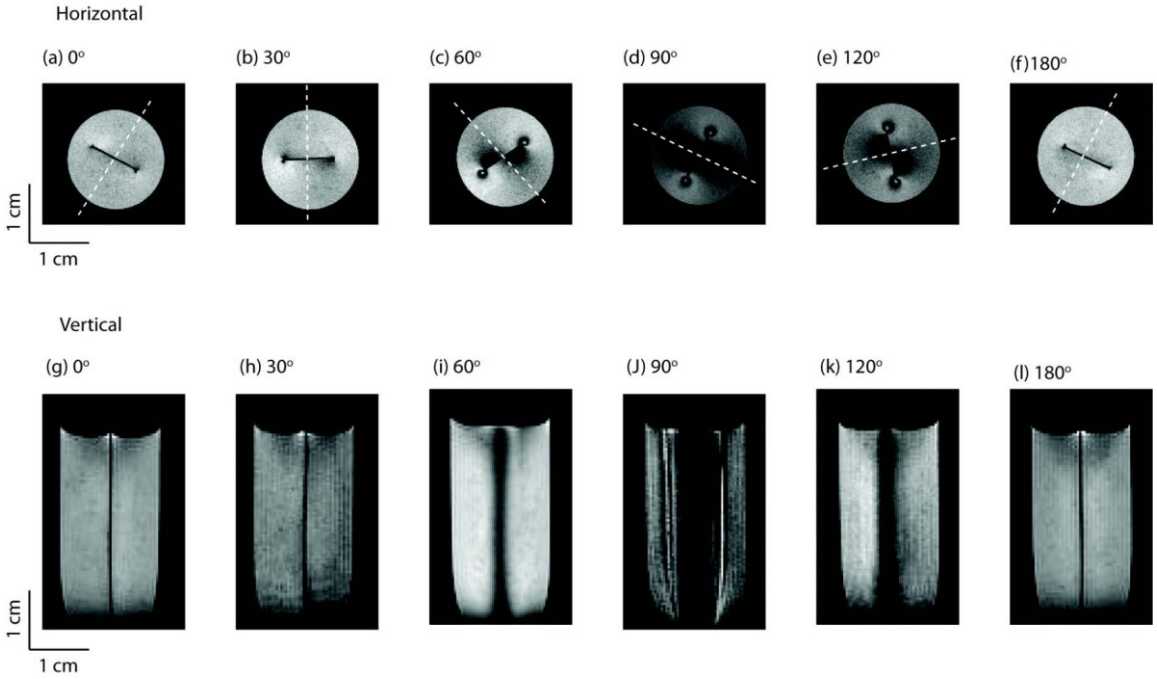

Figure 3.1. Horizontal spin density images (top) and vertical spin density images (bottom) of copper cell taken at different orientations with respect to the rf field. Figures 3.1a and 3.1f show horizontal images taken with the copper strip positions (0^o and 180^o respectively) aligned parallel to the rf radiation. Vertical images taken with the metal strip positioned parallel to the rf field (0^o and 180^o) are shown in figure 3.1g and 3.1l respectively. Both horizontal and vertical images labelled at 90^o orientation (figure 3.1d and 3.1j) were taken with the metal strip directly positioned perpendicular to the rf field. The dash white line on the horizontal (top) images indicates the region where the slice through the sample was taken to obtain the vertical images (bottom).

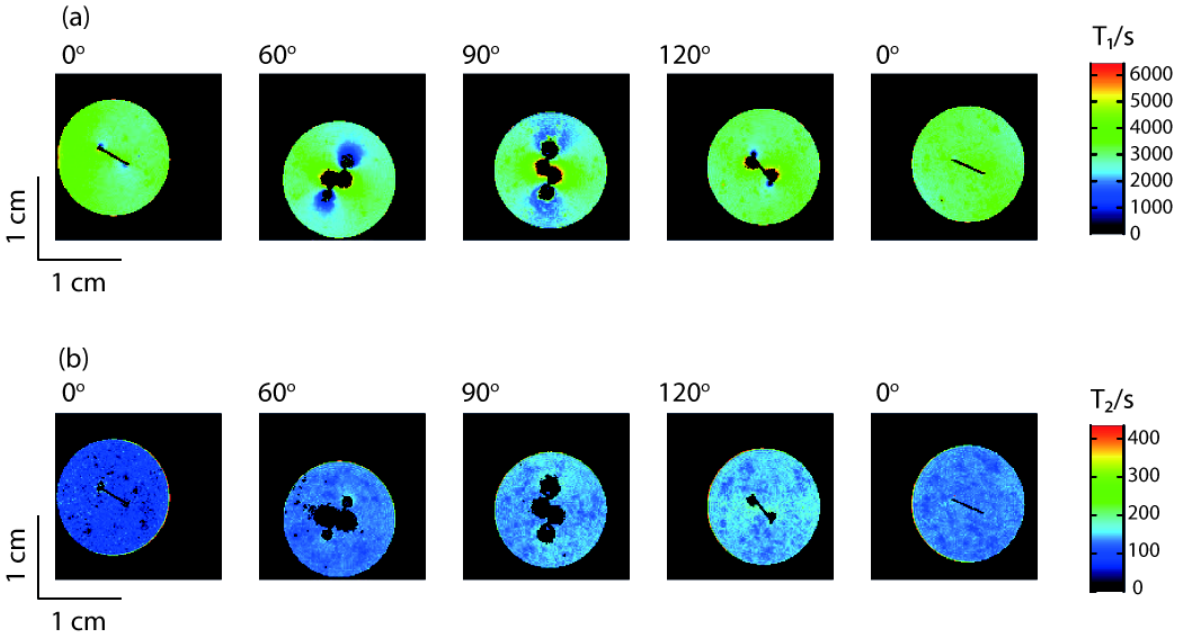

Figure 3.2. T_1 maps (a) and T_2 maps (b) of copper cell taken at different orientations with respect to the rf field. T_1 and *T_2* maps *taken with the metal strip positioned parallel to the rf field (0^o and 180^o) and those taken with the metal strip directly positioned perpendicular to the rf field are shown*

Figures 3.1**a** and 3.1**f** show horizontal spin density images taken with the copper strip positions (0^o and 180^o respectively) aligned parallel to the rf radiation. Vertical spin density images taken with the metal strip positioned parallel to the rf field (0^o and 180^o) are shown in figure 3.1**g** and 3.1**l** respectively. Horizontal T_1 and T_2 maps of the cell taken with the metal strip positioned at 0^o and 180^o (parallel position) are shown in figure 3.2 (a) and 3.2 (b) respectively. Both horizontal and vertical images labelled at 90^o orientation (figure 3.1**d** and 3.1**j**) were taken with the metal strip directly positioned perpendicular to the rf field. T_1 and T_2 maps of the cell labelled at 90^o orientation (figure 3.2) were taken with metal the strip aligned perpendicular to the rf field.

The spin density images (vertical and horizontal) and T_1 and T_2 maps, all show that the orientation of metals with respect to the rf field has significant effect on the appearance and quality of the images obtained. As seen from the spin density images and maps (figure 3.1 and 3.2), cells oriented parallel to the rf field direction (0^o and 180^o) give rise to little or no artefact while those oriented perpendicular (especially the 60^o and 90^o orientations) to the rf fields, show several artefacts. It can be seen from the images that as the copper strip is tilted away from parallel position (0^o and or 180^o) with respect to the rf field, the signal intensity near the metal starts to reduce and the image becomes more blurry. When the metal strip position is completely perpendicular to the rf field, at 90^o orientation, the signal intensity near the object is strongly reduced and the images become completely blurred and distorted. The perpendicular orientations do not only produce artefacts but also artificially alter the T_1 and T_2 of the gel electrolyte near the metal. This can clearly be seen in the T_1 and T_2 maps (figure 3.2) at 60^o and 90^o orientations. There is variation in the relaxation times of the electrolyte near the metal where the intrinsic relaxation times should be the same. These changes are much more sensitive to T_1 than T_2. Copper metal is a soft magnetic material (has magnetic compatibility of some kind and produce no easily detected forces when placed close to imaging region) hence it will have negative susceptibility and high electrical conductivity and as a result, rf artefacts will tend to dominate magnetic susceptibility artefacts. At antiparallel orientation to $\boldsymbol{B}_0$, (especially at 90^o, figures 3.1**d**, 3.1**j** and 3.2), the magnetic rf component $\boldsymbol{B}_1$ will induce a current loop around the copper strip, as a result the uniformity of the $\boldsymbol{B}_1$ exciting field is perturbed[49,52]. These variations in excitation angle which are believed to be due to a variation in the strength of the rf field make considerable artefacts to appear, and lead to poor visualization of the electrolyte near the metal (image distortion). Also, at perpendicular orientation, the

correlated $\boldsymbol{E}_1$ field will accelerate the copper electrons. This enhances the current density on the copper metal, resulting in the distorted images in figures 3.1**d** 3.1**j** and 90^o orientations in figure 3.2. For the imaging experiments of the cell, the copper strip position was oriented as parallel as possible with respect to the rf field in order to minimise artefacts associated with eddy current and rf shielding.

3.2 T_1 and T_2 maps of the copper cell

Two different time series of T_1 and T_2 maps of the copper corrosion cell taken at regular intervals over a period of 11 days are shown in figures 3.3 and 3.4.

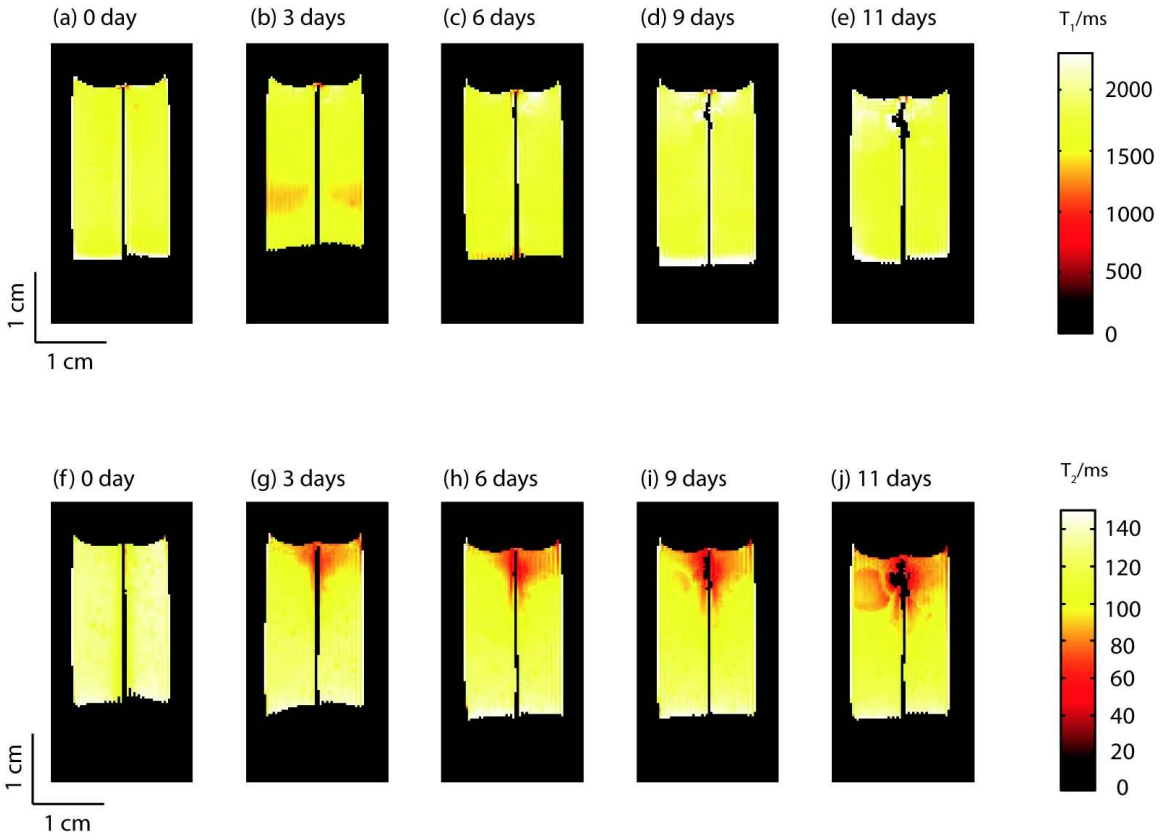

Figure 3.3. A time series of the first set of T_1 maps (top) and T_2 maps (bottom) of water during spontaneous corrosion of copper. The day's intervals during which images are acquired are shown. T_2 is found to decrease as the concentration of copper increases, while T_1 is not found to change significantly with increasing copper concentration.

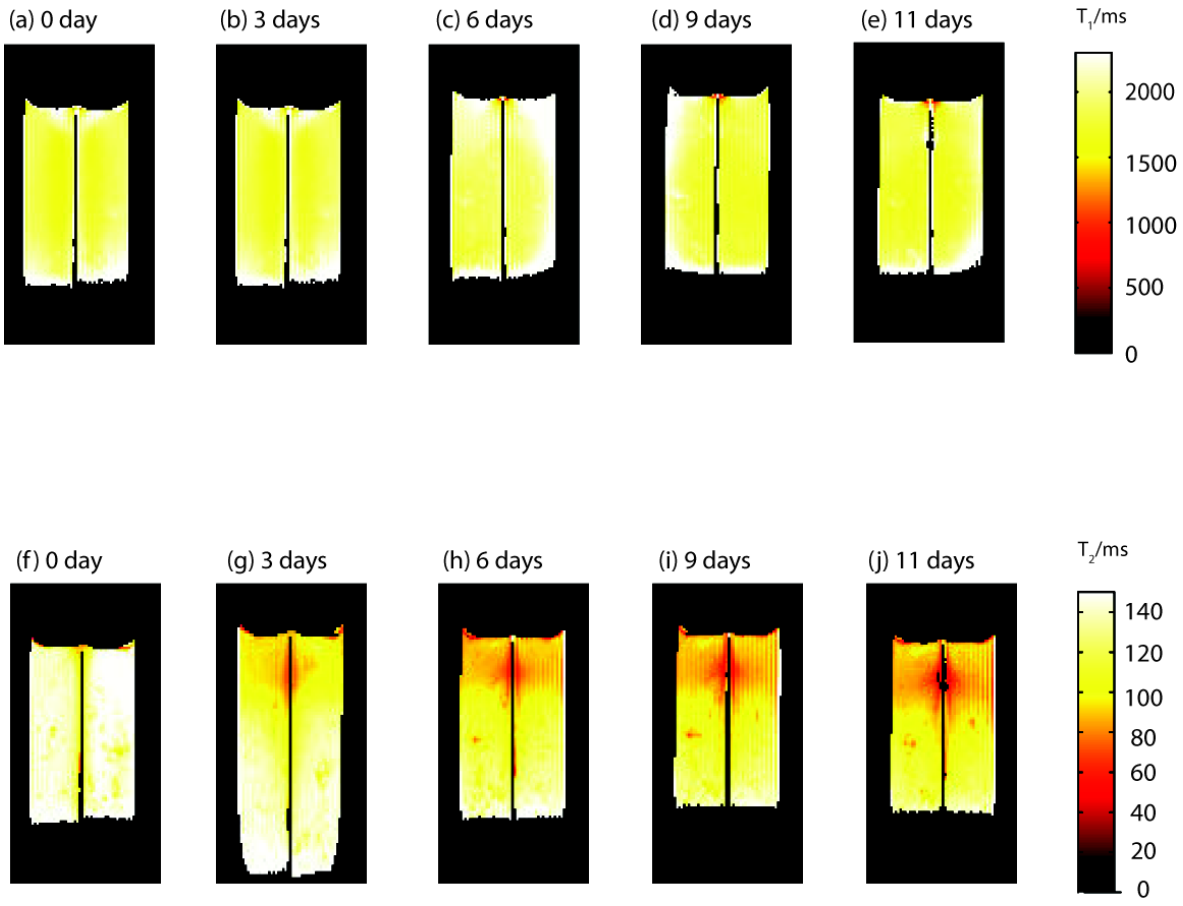

Figure 3.4. A time series of the second set of T_1 maps (top) and T_2 maps (bottom) of water during spontaneous corrosion of copper. The day's intervals during which images are acquired are shown. Figure 3.4 (g) appeared longer because during the image acquisition there was some signal reception issues and the coil had to be removed, readjusted and replaced. This caused the image to appear longer than the others. T_2 is found to decrease as the concentration of copper increases, while T_1 is not found to change significantly with increasing copper concentration.

The first time series of the T_1 and T_2 maps are shown in figure 3.3 and the second time series are shown in figure 3.4. The second time series was a repeat experiment of the first one. In both time series, T_2 is found to decrease as the concentration of copper increases

during spontaneous corrosion of the copper strip. Unlike T_2, T_1 was not found to change significantly during this process.

Figures 3.5 and 3.6 show photographs of the first and second corrosion cells as shown in figures 3.3 and 3.4 respectively.

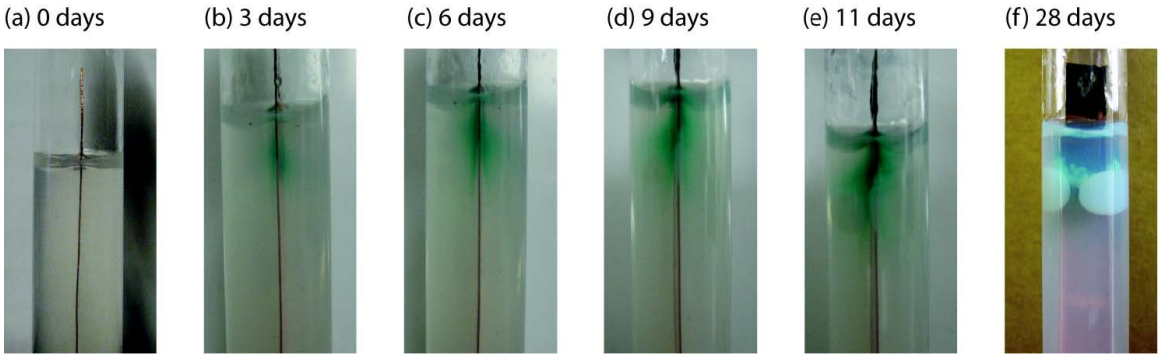

Figure 3.5. Photographs of the first set of copper strip in 0.5 M NaCl and 1.5 % w/v agar over time.

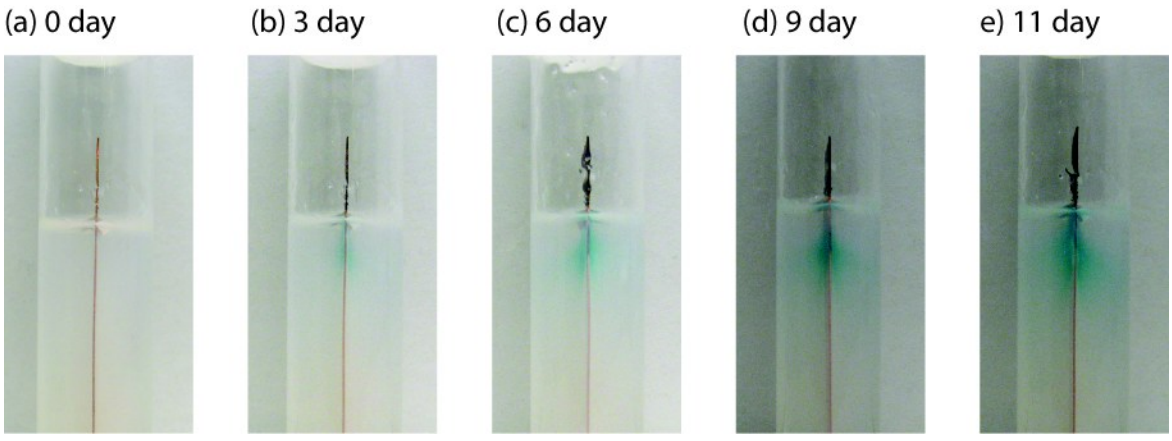

Figure 3.6. Photographs of the second set of copper strip in 0.5 M NaCl and 1.5 % w/v agar over time

As clearly seen from these photographs, the intensity of the greenish colour increased and spread across the width of the tube from day zero to day eleven. This is an indication that as the copper metal corrodes; Cu^{2+} ions get into the solution and diffuse across the tube.

T_1 profiles of relaxation time vs position for both set of experiments are given in figures 3.7 3.8. The T_1 profiles (figures 3.7 and 3.8) for both sets of experiments do not show any regular trend in the T_1 gradient.

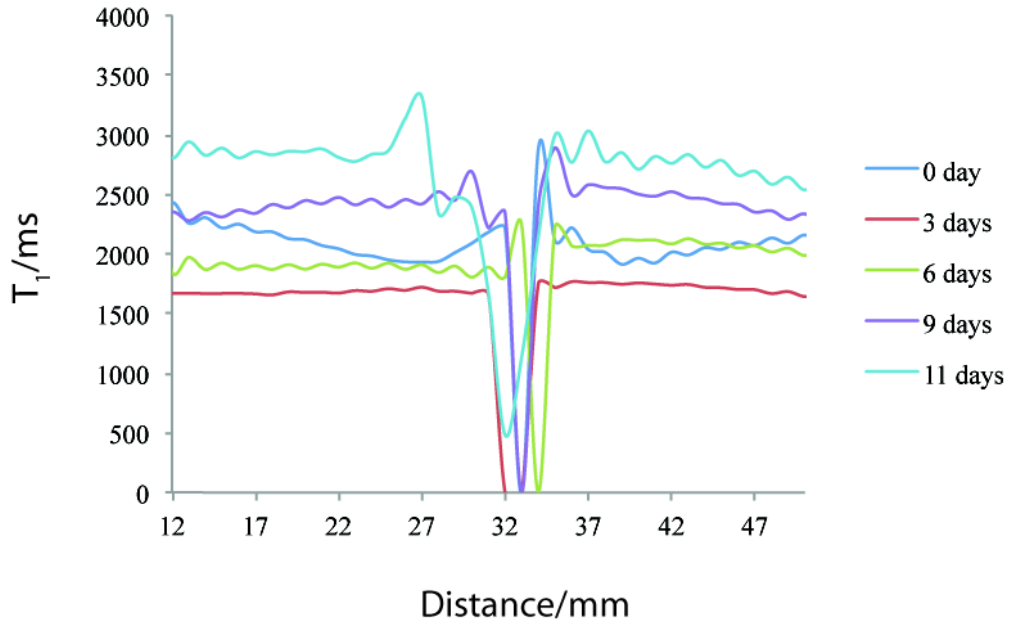

Figure 3.7. A time series of T_1 relaxation times profiles for the first set of T_1 maps taken along the width of the cell. Profiles are obtained by averaging 25 columns from the top of the cell over the full width where the corrosion seems to be more prominent.

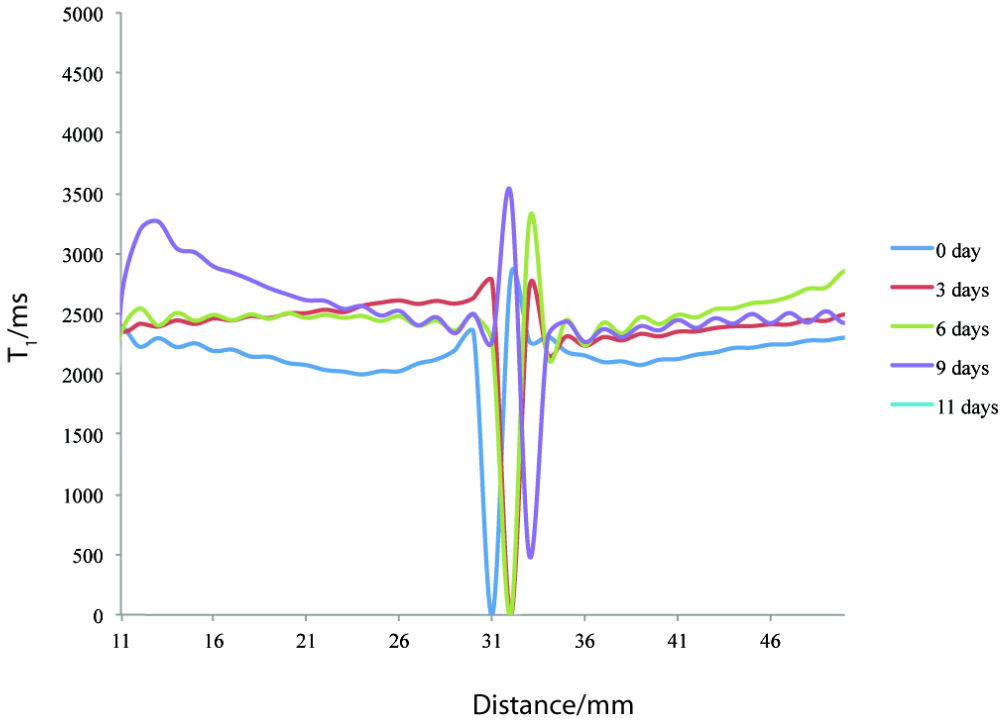

Figure 3.8. A time series of T_1 relaxation times profiles for the second set of T_1 maps taken along the width of the cell. Profiles are obtained by averaging 25 columns from the top of the cell over the full width where the corrosion seems to be more prominent.

Figures 3.9 and 3.10 show the T_2 profiles of relaxation time vs position for both set of experiments. The gradient in T_2 can clearly be seen in the T_2 profiles (figures 3.9 and 3.10)

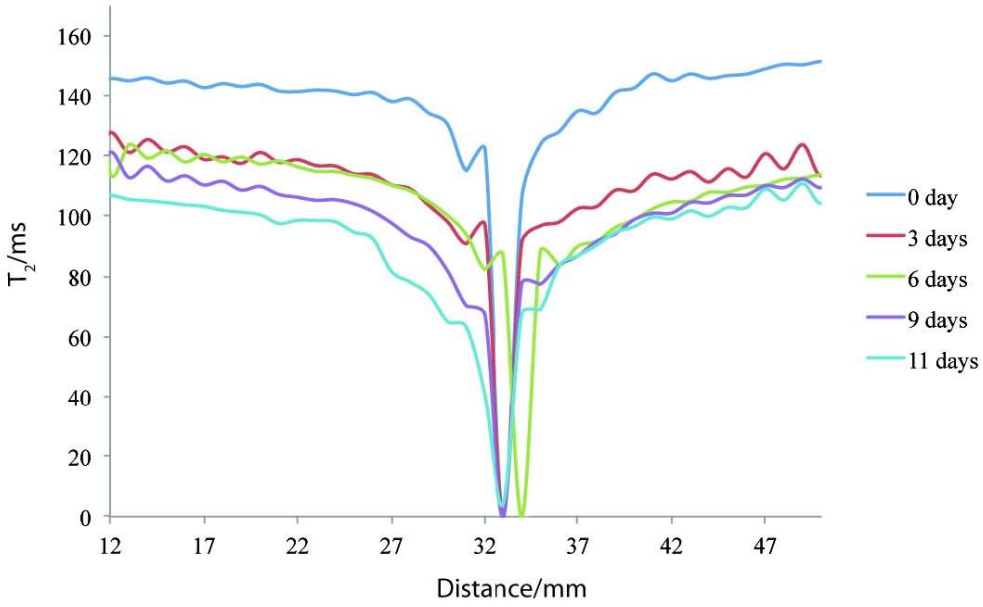

Figure 3.9. A time series of T_2 relaxation times profiles for the first set of T_2 maps taken along the width of the cell. Profiles are obtained by averaging 25 columns from the top of the cell over the full width where the corrosion seems to be more prominent.

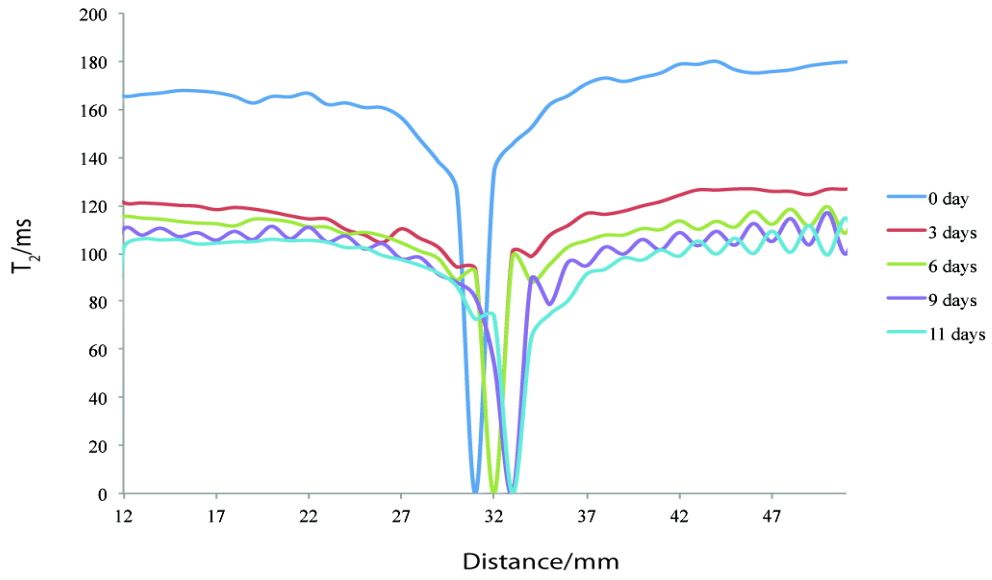

Figure 3.10. A time series of T_2 relaxation times profiles for the second set of T_2 maps taken along the width of the cell. Profiles are obtained by averaging 25 columns from the top of the cell over the full width where the corrosion seems to be more prominent.

In the T_2 relaxation maps for both set of experiments (figures 3.3**f-j** and 3.4**f-j**), it can be seen that there are major changes in the relaxation behaviour of the electrolyte (topmost

part) near the metal in solution as spontaneous corrosion of the copper strip occurs. The features in the T_2 maps for the first and second experiments are not exactly the same but there are marked similarities in the behaviour of both electrolytes. For instance it can clearly be seen that the images at 0 day for both T_2 maps (figures 3.3**f** and 3.4**f**) all show no observable changes in T_2 values of the electrolyte near the copper strip. After three days, (figures 3.3**g** and 3.4**g**), it can clearly be seen that regions at both sides of the copper strip show significant reduction in T_2. The reduction in T_2 is more wide-spread across the tube in the second T_2 maps (figure 3.4) than in the first T_2 maps (figure 3.3). Some stripe like features at the far top right hand corner of the tube are clearly visible in both sets of T_2 maps. These could be some kind of image artefacts appearing due the presence of the copper metal.

The variations in T_2 can easily be observed in the T_2 profiles (figures 3.9 and 3.10), showing a drastic fall across the width of the tube after 3 days. The drastic fall from day 0 to day 3 observed in both sets of T_2 profiles (figures 3.9 and 3.10) could be as a result of curing of the gel (gelation) and not entirely due to the presence of copper ion from corrosion. Subsequent fall (less drastic) in the T_2 variations can also be observed in the T_2 profiles after days 6,9 and 11 as shown in the T_2 maps in figures 3.3 and 3.4**h**, **i** and **j** respectively. The T_2 decreases across the width of the tube during the period of 6 and 9 days (figure 3.3**h** and 3.4**h** and 3.3**i** and 3.4**i**, respectively) until when it became nearly uniform across the topmost part of the tube at day 11 (figures 3.3 and 3.4**j**) where the signal started to die away near the copper strip as a result of the thickening of copper corrosion product formed around it. The cell photographs in figures 3.5 and 3.6**a**-**f** also show the same trend. The photographs for 0 day (figures 3.5 and 3.6**a**) show no greenish colour at all around the copper strip, but after three days, greenish colour starts to appear

across the width of the cell as seen in figures 3.5**b** and 3.6**b** which show that spontaneous corrosion of the copper strip has started to intensify after several days. As the copper metal corrodes over time, more and more Cu^{2+} ions get into the solution and that is responsible for the appearance of the greenish colour shown in the photographs. The spread in the greenish colour in the photographs correspond to the changes in the T_2 times of the electrolytes seen in the T_2 maps of both sets of experiments. A pale greenish (whitish) corrosion product in form of a circle appeared across the cell and this is made visible when the cell photograph is taken against a brown background as shown in figure 3.5**f.** This is also visible in the T_2 map taken after 11 days (figure 3.3**j**). A much shorter T_2 is observed around the greenish area in the T_2 map shown in figure 3.3**j.** A reduction in the T_2 around the whitish area is also observed but not to the same extent as the greenish area.

Little or no changes in the T_1 relaxation behaviour of the electrolytes is observed in both set of the T_1 maps (figures 3.3**a-e** and 3.4**a-e**). To show whether the T_1 maps represent the true relaxation times of the system, plots of the T_1 decay of different pixels showing relaxation times per pixels within the cell were taken for all the T_1 maps in the first set of experiments. Four different plots per T_1 map in figure 3.3 (showing off sets) taken at the top most part of the tube with their relaxation times are given in figures 3.11 and 3.12, for day 0 and day 11 respectively. The T_1 decays of the four pixels labelled **a**, **b**, **c** and **d** on the map**s** are shown. At the end of each decay, the signals are almost fully relaxed. Similar results were obtained for imaging experiments carried out for day 3, 6 and nine (figure 3.3) and all imaging experiments in figure 3.4. The relaxation times of the pixels do not show any significant changes for the maps from day 0 (when the corrosion started) to day 11 for all the T_1 maps. From the fits of the plots and the values of the relaxations times of all the

maps which do not show much variation, we can conclude that the T_1 times represents the reasonable relaxation times of the system.

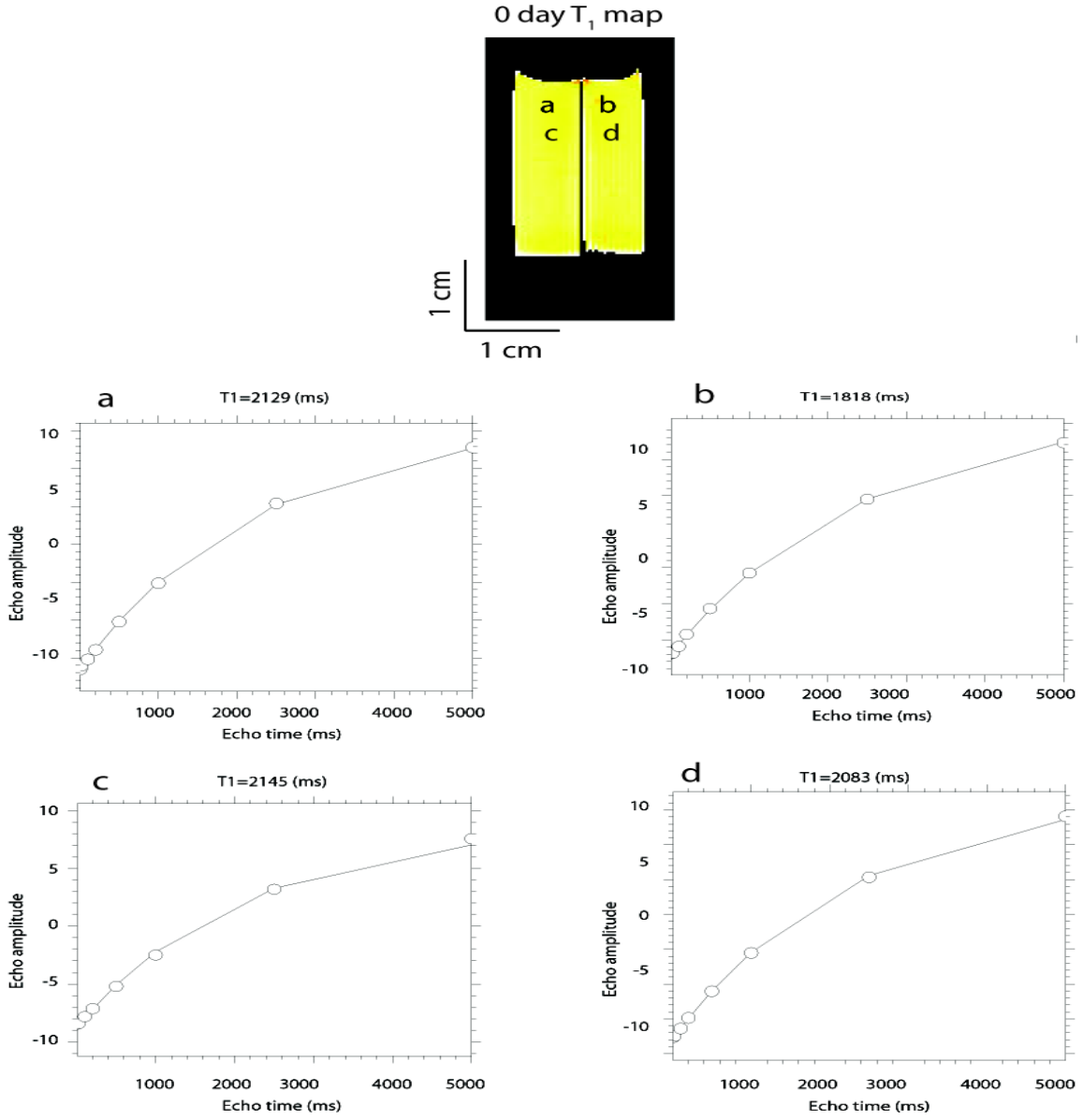

Figure 3.11. Plots of T_1 decays of pixels (showing off sets) within the T_1 maps for 0 day. Positions of the pixels are indicated in the map as shown using letters (a), (b), (c) and (d).

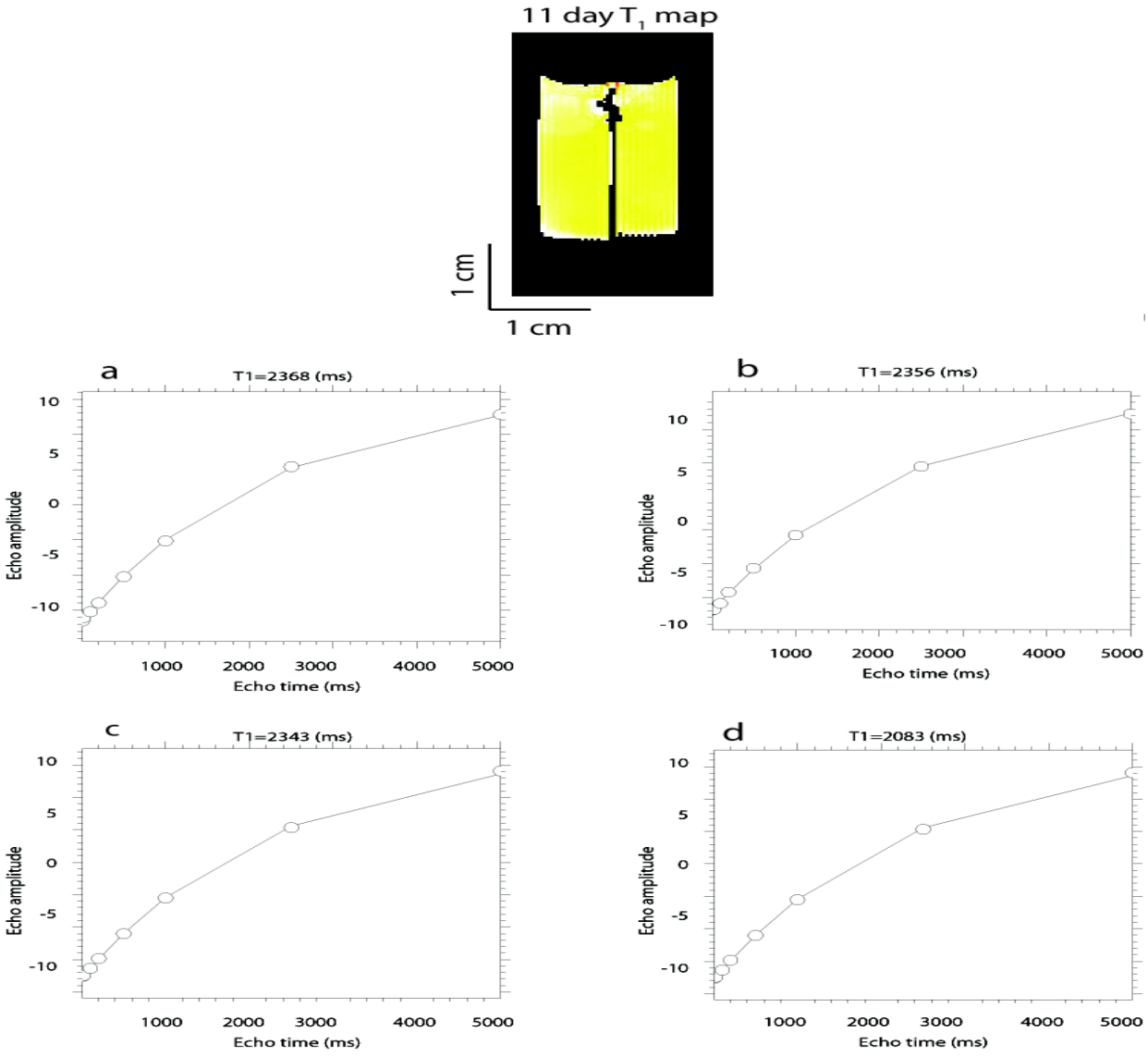

Figure 3.12. Plots of T_1 decays of pixels (showing off sets) within the T_1 maps for 11 day. Positions of the pixels are indicated in the map as shown using letters (a), (b), (c) and (d).

3.3 Relaxation maps of $CuSO_4$ solutions in NaCl/agar gel

T_1 and T_2 maps of $CuSO_4$ solutions in sodium/agar gel (the control samples) are shown in figure 3.13 (a) and (b) respectively. The T_1 and T_2 maps of varying $CuSO_4$ solutions in

sodium/agar gel show the dependence of magnetic resonance relaxation times on varying copper concentrations.

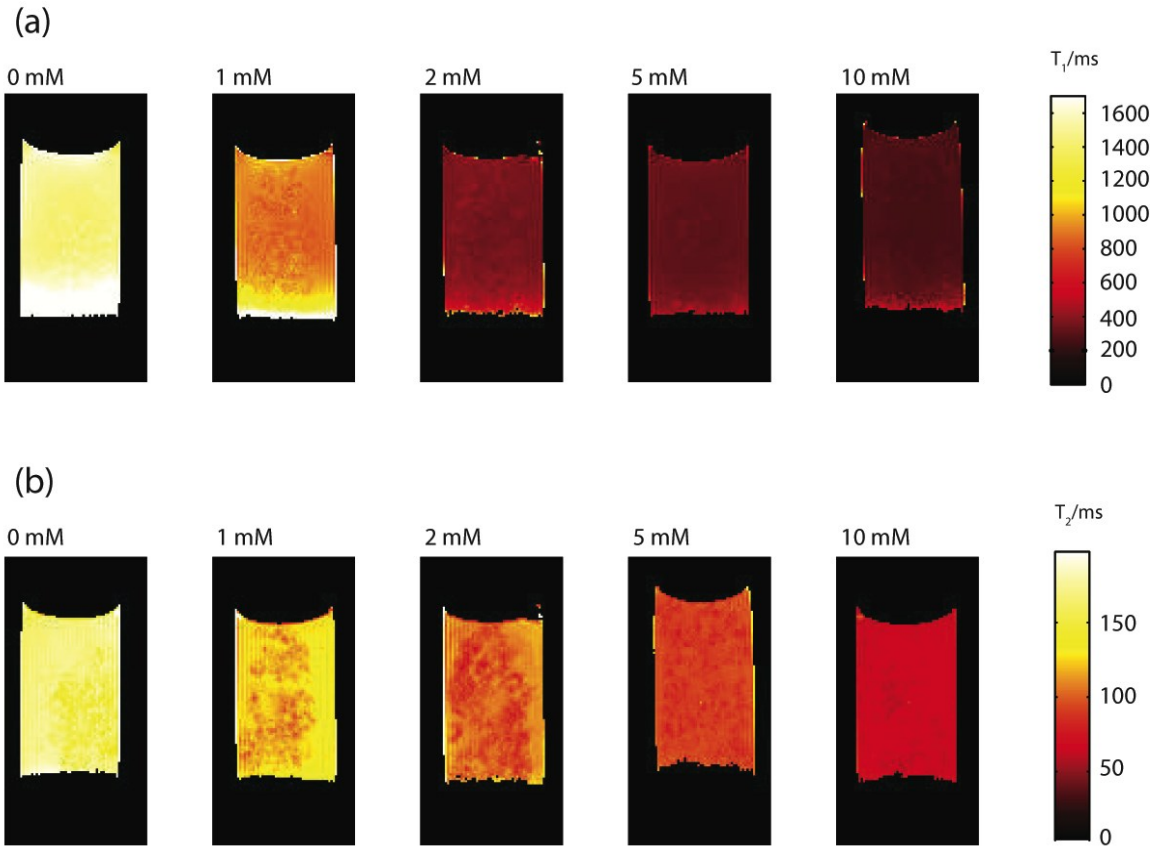

Figure 3.13 a) T_1 maps and b) T_2 maps for varying copper sulphate concentrations in 0.5 M sodium chloride and 1.5 % w/v agar. Both the T_1 and T_2 decrease with increase copper concentration.

As shown from the control maps, both the T_1 and T_2 times of the control sample decrease with increasing copper concentration. Inhomogeneous distribution of copper ions is observed in the control maps at lower copper sulphate concentrations due to the gel. This is more visible in the T_2 map at 1 mM and 2 mM concentrations.

T_1 and T_2 relaxation times were extracted from the control maps by averaging the relaxation times of all pixels (from the top of the tube to the area close to the bottom) as shown in figure 3.14. This is done for all the control maps of different copper concentrations. The average relaxation rates were then plotted against the different copper concentrations. The plots of average T_1 and T_2 relaxation rates of pixels within regions of the control maps as a function of different copper concentrations are shown in Figures 3.15 and 3.16 respectively. The average T_1 and T_1 relaxation rate also increase with increasing copper concentration.

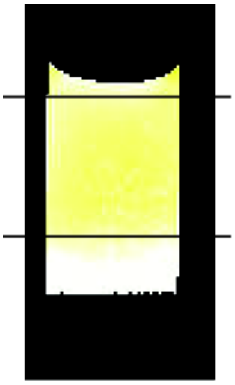

Figure 3.14. Control map showing region (top line down to bottom line) where relaxation times of pixels are averaged. This was applicable to all the T_1 and T_2 control maps in figure 3.13.

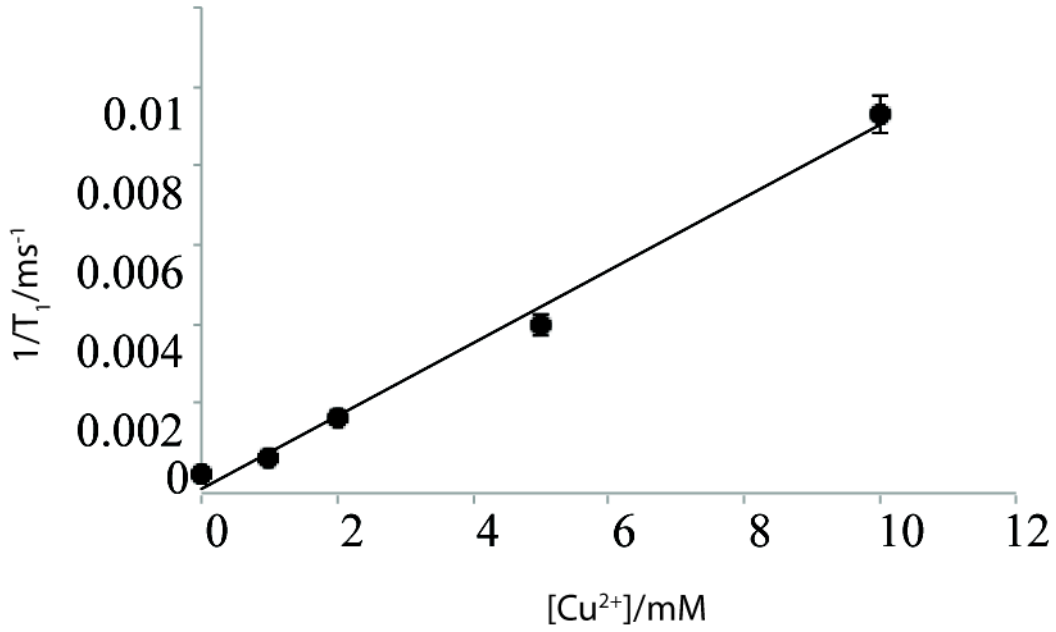

Figure 3.15. Average T_1 relaxation rates of pixels within regions of the control maps as a function of different copper concentrations in 0.5 M sodium chloride and 1.5 % w/v agar. Average T_1 relaxation rate increases with increasing copper concentration.

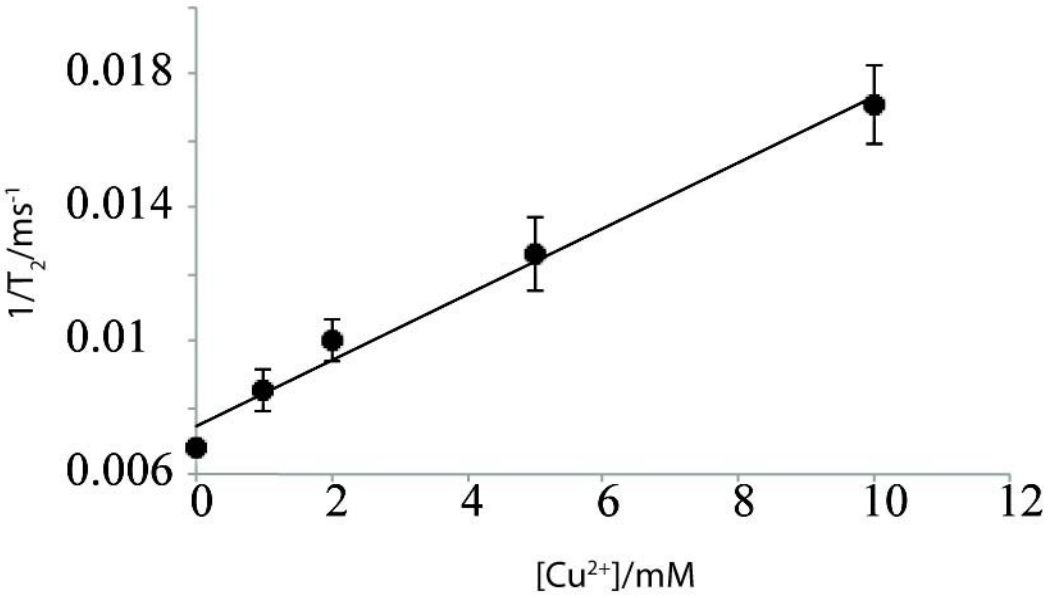

Figure 3.16. Average T_2 relaxation rates of pixels within regions of the control maps as a function of different copper concentrations in 0.5 M sodium chloride and 1.5 % w/v agar. Average T_2 relaxation rate increases with increasing copper concentration.

Bulk relaxation measurements of the control sample maps were carried out and an inverse of the relaxation times (relaxation rate) of the maps were plotted against different copper concentrations. Figures 3.17 and 3.18 show plots of bulk spin-lattice relaxation rate, $1/T_1$ and spin-spin relaxation rate, $1/T_2$ of the control maps against different copper sulphate concentrations respectively.

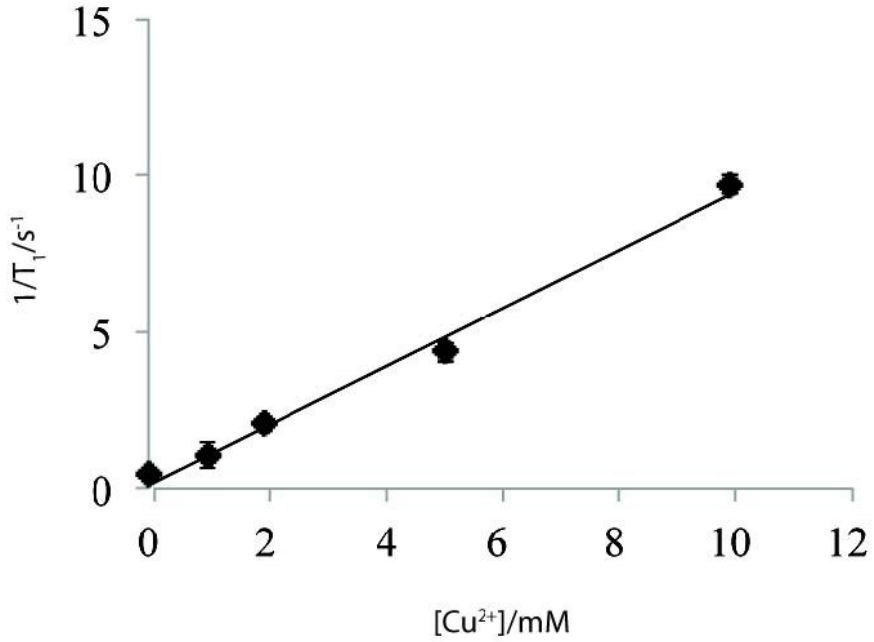

Figure 3.17. Bulk T_1 relaxation rates for solutions of copper sulphate in 0.5 M sodium chloride and 1.5 % w/v agar. T_1 relaxation rate increases with increasing copper concentration.

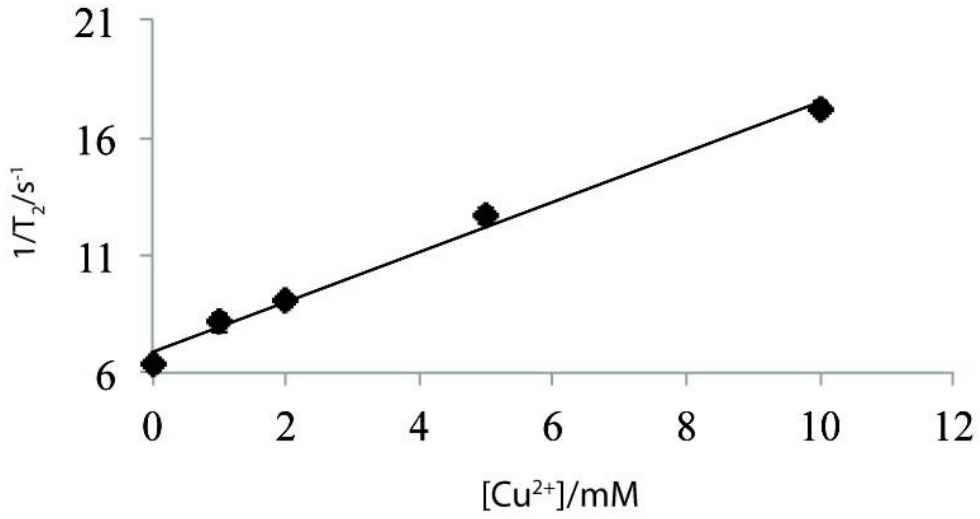

Figure 3.18. Bulk T_2 relaxation rates for solutions of copper sulphate in 0.5 M sodium chloride and 1.5 % w/v agar. T_2 relaxation rate increases with increasing copper concentration.

The trend of the bulk relaxation measurements (figures 3.17 and 3.18) are in agreement with changes shown in the relaxation maps (figure 3.13) and average relaxation times measurements (figures 3.15 and 3.16). Relaxation measurements of varying copper concentrations in 0.5 M sodium chloride and 1.5 % w/v agar (control samples) were carried out to show the effects of increasing copper concentration on the relaxivity of proton water molecules in the copper corrosion system. As shown in all the relaxivity plots, the relaxation rate of the control sample solution is linearly dependent on the concentration of paramagnetic copper ions (equation 1.22). The relaxivities of the T_1 and T_2 maps calculated from the graphs are approximately 0.001 $mM^{-1}s^{-1}$. This is consistent with previous relaxation measurements, indicating correlation between relaxation rates and copper ion concentrations in the solution[62]. Both the bulk relaxation time measurements

and the average relaxation times of pixels within regions of the control maps show the same trend. The equation obtained from these linear fits (equation 1.22) can be used to quantitatively determine concentrations of copper ions in the solutions. So by extension, the relaxation times of systems can be used to determine the concentrations of paramagnetic ions present in the system.

As seen from both the bulk and average T_1 and T_2 relaxivity plots (figures 3.14, 3.15 ,3.16, and 3.17), the relaxation rate of water molecules in the copper sulphate solution increases with increasing copper concentration. This means that as the concentration of copper ions increases in the solution, the T_1 and T_2 relaxation times decrease. This can clearly be seen in the control sample maps in figure 3.16 **a** and **b** respectively. Paramagnetic copper ions are found to reduce the relaxation times of water molecules surrounding them[1,30,55]. Substantial reductions in spin-spin and spin-lattice relaxation times of water protons near the vicinity of the copper ion should be observed due to decreased mobility and exchange processes[30]. The reason is that unpaired electrons in paramagnetic copper ions bring about localised magnetic field fluctuations that enhance the relaxation rate of solvent nuclei in their vicinity. Enhancement of the relaxation rate will normally be achieved through inner-sphere and outer-sphere exchanges processes or mechanisms as explained in section 1.8.1 of this work. Neighbouring water molecules will form co-ordination shells around copper ions in the solution and as a result, the molecular correlation time of the water molecules will be reduced (i.e water molecules tumble slowly through the solution). This will enhance their relaxation rate (increase relaxivity) and hence an increase in their T_1 and T_2 relaxation times. For simple systems, there is a linear relationship between the relation rate of water protons and the paramagnetic concentration (equation 1.22). This linear relationship is demonstrated in the bulk and average T_1 and T_2 relaxivity plots (figure 3.17-

3.20). As explained earlier (section 1.8.1) using equation 1.21 and 1.22, the relaxation rates of the system (control maps) are not entirely from paramagnetic contribution. In the absence of paramagnetic copper ions (at zero copper concentration), the relaxation rate in all the plots are not zero, which means that there is also diamagnetic contribution from water molecules and gel in the solution.

The T_2 maps in figure 3.2**f-j** show a clear variation in the electrolytes solution during spontaneous corrosion of the copper strip. A change in the electrolyte solution is clearly visible after three days of corrosion. An initial increase in Cu^{2+} concentration in the electrolyte solution is expected to give rise to a decrease in relaxation time of the water molecules surrounding the ions in the copper corrosion cell. This phenomenon is clearly seen for T_2 maps of the corrosion cell, but not seen in T_1 maps. As expected, the presence of paramagnetic Cu^{2+} in the system gives rise to reduction of the T_2. This is as a result of exchange processes and decreased mobility as explained in the discussion earlier.

As the copper strip corrodes, Cu^{2+} ions enter the solution and neighbouring water molecules form solvation shells around them and the protons spin relaxation of these solvent molecules are enhanced significantly compared with those of the bulk water[63]. Paramagnetic copper ion in the solutions would lead to increased molecular correlation time and decreased mobility of the surrounding water molecules; hence the relaxation rate of the protons in the water molecules will increase[30].

In a sodium chloride solution, the copper metal would be oxidised firstly by associating

with Cl^- to give a $CuCl_2$ complex in the solution[15,16]. Dissolution of this complex will proceed in the solution to give Cu^{2+} [13,16] which is expected to lead to a reduction in T_2 times as clearly seen in the T_2 maps of the corrosion cell. Meanwhile, copper can as well

be oxidised to give cuprite, Cu_2O, which will in turn be oxidised to Cu^{2+} in the presence of water molecules according to the following half-electrochemical reactions in equations 3.1 and 3.2[8,13,16]:

$$Cu^{+} \rightarrow Cu^{2+} \qquad (3.1)$$

$$0.5O_2 + H_2O + 2e \rightarrow 2OH^{-} \qquad (3.2)$$

This can also lead to further decrease in T_2 of the electrolyte near the metal strip across the width of the tube as seen in the T_2 maps. Hydrolysis of the Cu^{2+} in the presence of Cl^{-} would lead to the formation of some corrosion products. Tribasic copper chloride known as paracetamite $[Cu_2(OH)_3Cl]$[13,25,64,65] has been identified as the final corrosion product in this copper corrosion cell. The identification was done using X-ray diffraction analysis which shows the presence of sodium chloride and the paratacamite as shown from the X-ray patterns in figure 3.19. Two peaks (blue and red) are identified in the x-ray pattern, the red peak is due to sodium chloride and the blue peak shows the presence of paratacamite. Some other corrosion products have been identified in similar systems using identifications techniques other than x-ray diffraction analysis. Difficulties in separating the greenish and whitish corrosion products (copper compounds) in the corrosion cell prior to the X-ray diffraction analysis and also the drying process might have led to the lost of some corrosion products. This could possibly be the reasons why some of the expected copper compounds were not identified by X-ray diffraction technique. Also non- crystalline products present cannot be identified by X-ray techniques. The presence of these corrosion products could possibly be the reason why variation in the T_1 times was not readily visible in the T_1 maps (figures 3.3 and 3.4**a-e**). This conclusion is drown from the fact that in the T_1 controls maps (figure 3.5**a)**, even in the presence of the gel and sodium chloride,

relaxation time of the proton water molecules is found to decrease with increasing copper concentration due to the presence of copper ions. This shows that presence of these species (gel electrolyte) will not significantly affect the T_1 rate. As shown in the T_1 relaxivity plots, they can only give some diamagnetic contributions to the system. T_1 relaxation is strongly dependent on water coordination to the paramagnetic copper ions as described in equation 1.23. . Unlike the copper corrosion cell, in the control samples the paramagnetic metal centre will have numerous coordination sites (higher number of bound water molecules, q) since there will be no corrosion products. These bound water protons will be in fast exchange with the bulk solvent (short residence time, τ_M) and the effects of the paramagnetic contrast agent will be greater, hence the relaxation time will be decreased significantly with increasing copper concentration (higher relaxivity) as seen in the T_1 control maps in figure 3.1 (a). The tribasic copper chloride and other corrosion products that might be present in the system could affect the change in the T_1 times as shown in the T_1 maps. The tribasic copper chloride complex (paratacamite) contains no inner-sphere water molecules; it has non-accessible coordination site i.e zero number of bound water molecules (q=0) to the metal centre. For this reasons, there will be no interaction between the paramagnetic metal centre and the bulk solvent. Without exchange of water protons between the copper metal and the bulk solvent, the paramagnetic effect of the copper will be very minimal or negligible since T_1 is strongly dependent on inner-sphere relaxation. This would lead to slower relaxation rate and hence low relaxivity. This could possibly be the reason why little or change was observed in the T_1 maps. The reduction observed in the T_2 times of the copper corrosion cell shown in the T_2 maps is due to the contribution from the outer-sphere relaxation mechanisms (equation 1.23), in which the relaxivity generally

depends on the distance of closest approach of outer-sphere water protons, *d,* and the translational diffusion time τ_D, of the water molecules.

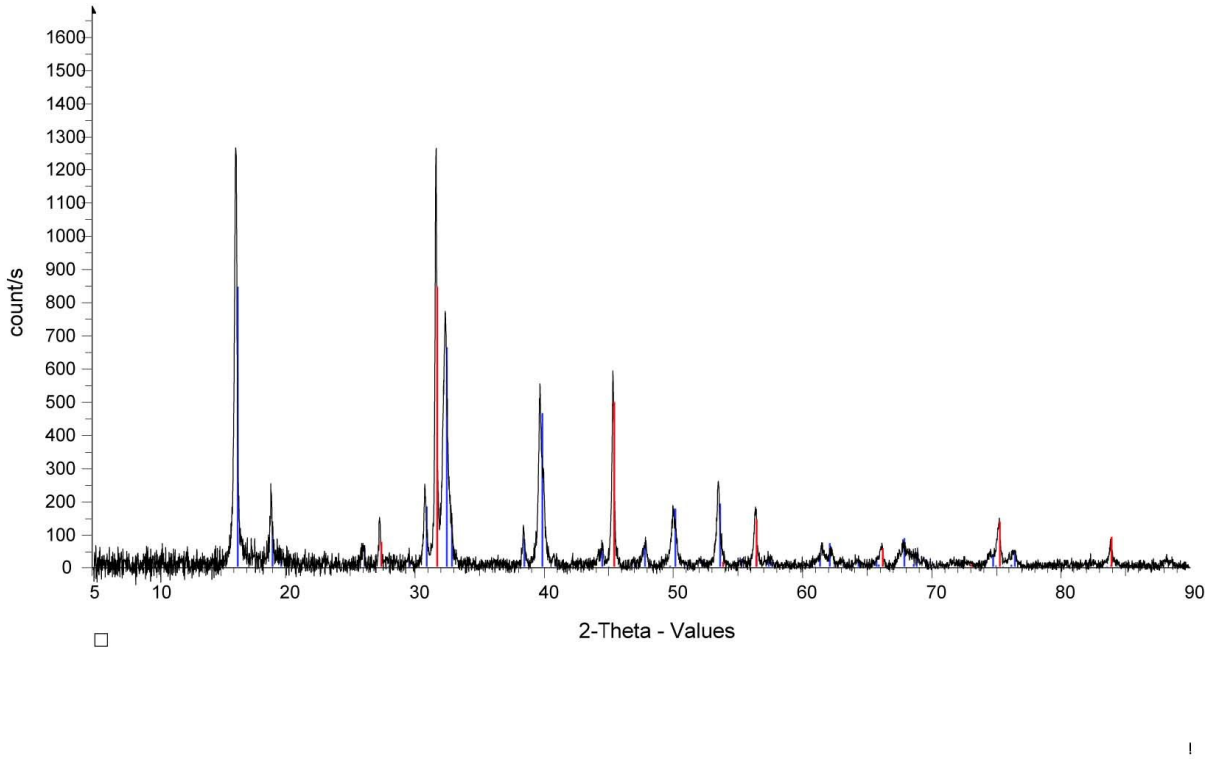

Figure 3.19. XRD pattern of the corrosion product showing paratacamite peaks (blue).

3.4 T_2 concentration maps

Figures 3.20 and 3.21 show time series of concentration maps produced from the two sets of T_2 relaxation maps in figures 3.3 and 3.4 respectively.

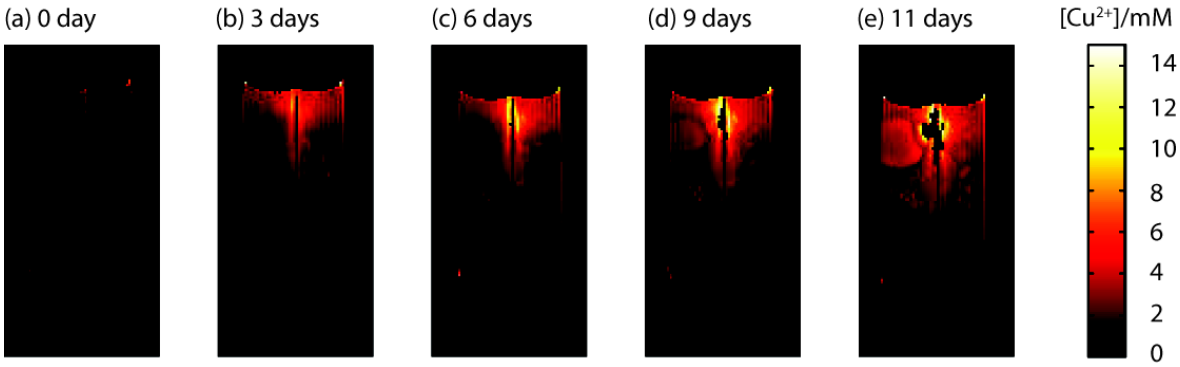

Figure 3.20. A time series of concentration maps produced from the T_2 relaxation map (figure 3.3). The concentration maps are extracted using the relationship between T_2 and $[Cu^{2+}]$ by transforming the T_2 value of each pixel in the T_2 maps into a copper concentration value using algorithm in prospa soft ware.

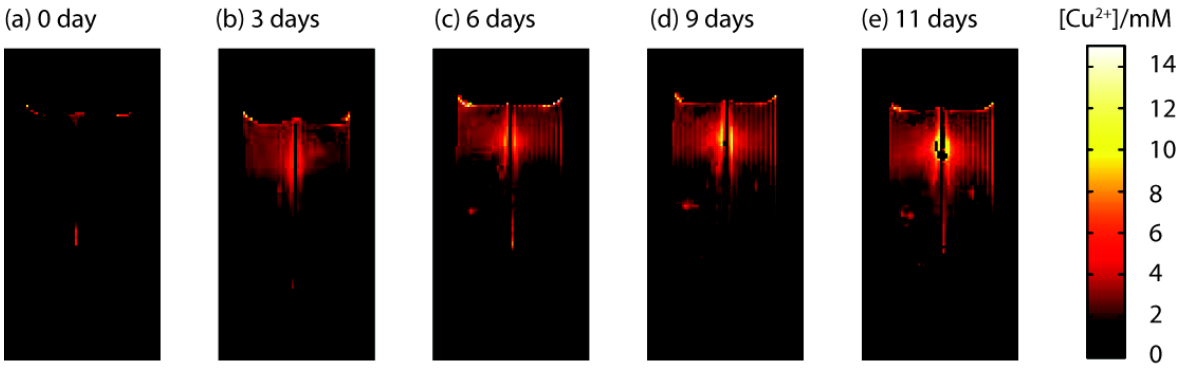

Figure 3.21. A time series of concentration maps produced from the T_2 relaxation maps (figure 3.4). The concentration maps are extracted using the relationship between T_2 and $[Cu^{2+}]$ by transforming the T_2 value of each pixel in the T_2 maps into a copper concentration value using algorithm in prospa software.

The concentration maps were produced using the relationship between T_2 and $[Cu^{2+}]$ in the straight line equation for the linear fit in figure 3.15. The T_2 value of each pixel in the T_2 maps was transformed into a copper concentration value. Copper ion concentration $[Cu^{2+}]$ was found to increase across the width of the tube from top to bottom as corrosion progresses.

Copper concentration in both the two T_2 concentration maps at day zero (figures 3.20 and 3.21) is near zero because the corrosion of the copper has barely started. As seen from these maps, they appear completely dark except for some features which could possibly be artefacts at the top of the tubes. As the copper strip corrodes further after 3 days, copper ions will diffuse across the tube and the concentration of copper ions increases in the solution and this can clearly be seen in the concentration map in figure 3.20**b** and 3.21**b**. The concentration increases further into the solution across the width of the tube from top half way to the bottom as seen in the concentration maps from day 6 up to day 11 (figures 3.20 and 3.21**c**, **d** and **e**). This copper ion concentration spread can also be seen in the cell photographs (appearance of greenish colour across the width of the tube) shown in figures 3.5 and 3.6**b**, **c**, and **d**. The phenomena shown in the concentration maps further explained the direct correlation between the concentration of paramagnetic copper ions and magnetic relaxation times of systems.

4 Conclusion and further work

MRI of a copper corrosion system has shown that the orientation of metals with respect to the rf field has a significant effect on the appearance and quality of images obtained from electrochemical systems. By selecting a two-dimensional strip of metal and orienting it parallel to $\boldsymbol{B}_0$ and $\boldsymbol{B}_1$, it was possible to minimise artefacts associated with eddy currents and rf shielding and acquire distortionless images for the electrolyte surrounding the copper.

The T_1 and T_2 relaxation measurements of varying copper concentrations in 0.5 M sodium chloride and 1.5 % w/v agar showed that the relaxation rate of proton water molecules increases with increasing copper concentration. Diamagnetic contributions from other species apart from copper ions to the relaxivity of proton water molecules in the system were also observed.

For the first time, MRI has been used to map the spatial distribution of copper ions and concentration during corrosion processes. Variation in T_1 and T_2 from the images was used to monitor spatial distribution of ions as well as changes in copper concentration in the aqueous salt solution. A time series of T_2 maps revealed the spatial distribution of copper ions during the process of copper corrosion. The T_2 concentration maps also showed how the concentration of copper ions increases as they are spatially distributed during the process. T_1 map did not exhibit any significant change during the process of copper corrosion. This could be due to the presence of some corrosion products formed in the copper corrosion cell over time. Dibasic copper chloride complex (paratacamite) with zero

inner-sphere water molecules has been identified by X-ray diffraction analysis. The presence of this copper complex might have affected the paramagnetic effect of the copper which will reduce the relaxivity of the bulk solvent and hence the particular T_1 behaviour observed in the system.

Careful separation method needs to be developed in further work in order for the corrosion products obtained to be separately analysed. Optimised drying method also should be device in order to retain all possible products formed during corrosion. X-ray energy dispersive spectroscopy, Raman spectroscopy and other relevant qualitative analytical techniques are still required to confirm non-crystals corrosion products that might be form in the copper corrosion cell.

This technique can as well be extended to map spatial distribution of metal ions and monitor changes in concentration in other electrochemical corrosion systems. The technique can also be applied to study other electrochemical systems and energy devices like batteries and fuel cells.

Development of MRI techniques that can be used to minimize susceptibility artifacts can also be required in order to probe systems with strong magnetic material eg Ni, steal etc.

References

(1) Britton, M. M. *Chemical Society Reviews* **2010**, *39*, 4036.

(2) Britton, M. M.; Sederman, A. J.; Taylor, A. F.; Scott, S. K.; Gladden, L. F. *Journal of Physical Chemistry A* **2005**, *109*, 8306.

(3) Evans, R.; Timmel, C. R.; Hore, P. J.; Britton, M. M. *Journal of the American Chemical Society* **2006**, *128*, 7309.

(4) Davenport, A. J.; Forsyth, M.; Britton, M. M. *Electrochemistry Communications* **2010**, *12*, 44.

(5) Chandrashekar, S.; Trease, N. M.; C., J.; Du, L.; Grey, C. P.; and Jerschow, A. *Nature Materials* **2012**, *11*, 311.

(6) Klett, M.; Giesecke, M.; Nyman, A.; Hallberg, F.; Lindstrom, R. W.; Lindbergh, G.; Furo, I. *Journal of the American Chemical Society* **2012**, *134*, 14654.

(7) Khaled, K. F. *Materials Chemistry and Physics* **2011**, *130*, 1394.

(8) El-Egamy, S. S. *Corrosion Science* **2008**, *50*, 928.

(9) Farzin, A.; Annemie, A. *Materials Chemistry and Physics* **2012**, *5*, 2439.

(10) Cong, H. B.; Scully, J. R. *Journal of the Electrochemical Society* **2010**, *157*, C200.

(11) Drogowska, M.; Brossard, L.; Menard, H. *Surface & Coatings Technology* **1988**, *34*, 383.

(12) Duthil, J. P.; Mankowski, G.; Giusti, A. *Corrosion Science* **1996**, *38*, 1839.

(13) Gamal, A. E. *Corrosion Science* **2005**, *47*, 1370.

(14) Khaled, K. F.; Hamed, M. N. H.; Abdel-Azim, K. M.; Abdelshafi, N. S. *Journal of Solid State Electrochemistry* **2011**, *15*, 663.

(15) King, F.; Quinn, M. J.; Litke, C. D. *Journal of Electroanalytical Chemistry* **1995**, *385*, 45.

(16) FitzGerald, K. P.; Nairn, J.; Skennerton, G.; Atrens, A. *Corrosion Science* **2006**, *48*, 2480.

(17) Cong, H. B.; Scully, J. R. *Journal of the Electrochemical Society* **2010**, *157*, C36.

(18) King, F.; Litke, C. D.; Tang, Y. *Journal of Electroanalytical Chemistry* **1995**, *384*, 105.

(19) Nassau, K.; Gallagher, P. K.; Miller, A. E.; Graedel, T. E. *Corrosion Science* **1987**, *27*, 669.

(20) Christy, A. G.; Lowe, A.; Otieno-Alego, V.; Stoll, M.; Webster, R. D. *Journal of Applied Electrochemistry* **2004**, *34*, 225.

(21) Drogowska, M.; Brossard, L.; Menard, H. *Journal of the Electrochemical Society* **1992**, *139*, 39.

(22) Lytle, D. A.; Schock, M. R. *Journal American Water Works Association* **2008**, *100*, 115.

(23) Ha, H.; Taxen, C.; Williams, K.; Scully, J. *Electrochimica Acta* **2011**, *56*, 6165.

(24) Kear, G.; Barker, B. D.; Walsh, F. C. *Corrosion Science* **2004**, *46*, 109.

(25) Graedel, T. E.; Nassau, K.; Franey, J. P. *Corrosion Science* **1987**, *27*, 639.

(26) Graedel, T. E. *Corrosion Science* **1987**, *27*, 721.

(27) Graedel, T. E.; Franey, J. P.; Kammlott, G. W.; Vandenberg, J. M.; Key, P. L. *Journal of the Electrochemical Society* **1987**, *134*, 1632.

(28) Ohno, D.; Iwai, Y. a. K., J. *Atom Indonesia* **2010**, *Volume 36*, 129.

(29) Deverell, C. *Progress in Nuclear Magnetic Resonance* **1969**, *4*, 235.

(30) Holz, M. In *Progresses in Nuclear Magnetic Resonance Spectroscopy*, 1986; Vol. 18; pp 327.

(31) Chevallier, F.; Letellier, M.; Morcrette, M.; Tarascon, J. M.; Frackowiak, E.; Rouzaud, J. N.; Beguin, F. *Electrochemical and Solid State Letters* **2003**, *6*, A225.

(32) Klod, S.; Dunsch, L. *Magnetic Resonance in Chemistry* **2011**, *49*, 725.

(33) Hertz, H. G. *Progresses in Nuclear Magnetic Resonance Spectroscopy* **1967**, *3*, 159.

(34) Marcus, Y. *Chemical Reviews* **2009**, *109*, 1346.

(35) Callaghan, P. T. *Principles of Nuclear Magnetic Resonance Microscopy*; Oxford University press: New York, 2006.

(36) Hore, P. J. *Nuclear Magnetic Resonance*; Oxford University Press: New york, 1995.

(37) Vadim, K. *MRI: Physical principles and Applcations*; Academic Press, 2000.

(38) Mark, A. B.; Richard, C. S. *MRI: Basic principles and Applications*, 3rd ed.; John Wiley and Sons, 2003.

(39) Freeman, R. Magnetic Resonance in Chemistry and Medcine; Oxford University Press: New york, 2003.

(40) Levitt, M. H. *Spin dynamics: Basics of Nuclear Magnetic Resonance*; John Wiley and Sons, 2002.

(41) Kangarlu, A.; Abduljalil, A. M.; Schwarzbauer, C.; Norris, D. G.; Robitaille, P. M. L. *Magnetic Resonance Materials in Physics Biology and Medicine* **1999**, *9*, 81.

(42) Koch, K. M.; Hargreaves, B. A.; Pauly, K. B.; Chen, W.; Gold, G. E.; King, K. F. *Journal of Magnetic Resonance Imaging* **2010**, *32*, 773.

(43) Schenck, J. F. *Medical Physics* **1996**, *23*, 815.

(44) Bennett, L. H.; Wang, P. S.; Donahue, M. J. *Journal of Applied Physics* **1996**, *79*, 4712.

(45) Koch, K. M.; Brau, A. C.; Chen, W.; Gold, G. E.; Hargreaves, B. A.; Koff, M.; McKinnon, G. C.; Potter, H. G.; King, K. F. *Magnetic Resonance in Medicine* **2011**, *65*, 71.

(46) Chen, C. A.; Chen, W. T.; Goodman, S. B.; Hargreaves, B. A.; Koch, K. M.; Lu, W. M.; Brau, A. C.; Draper, C. E.; Delp, S. L.; Gold, G. E. *Journal of Magnetic Resonance Imaging* **2011**, *33*, 1121.

(47) Zho, S. Y.; Kim, M. O.; Lee, K. W.; Kim, D. H. *Journal of Magnetic Resonance Imaging* **2013**, *37*, 471.

(48) Hargreaves, B. A.; Worters, P. W.; Pauly, K. B.; Pauly, J. M.; Koch, K. M.; Gold, G. E. *American Journal of Roentgenology* **2011**, *197*, 547.

(49) Graf, H.; Lauer, U. A.; Berger, A.; Schick, F. *Magnetic Resonance Imaging* **2005**, *23*, 493.

(50) Graf, H.; Steidle, G.; Lauer, U. A.; Schick, F. *Medical Physics* **2005**, *32*, 337.

(51) Malko, J. A.; Hoffman, J. C.; Jarrett, P. J. *Radiology* **1989**, *173*, 563.

(52) Bartels, L. W.; Bakker, C. J. G.; Viergever, M. A. *Magnetic Resonance in Medicine* **2002**, *47*, 171.

(53) Graf, H.; Steidle, G.; Martirosian, P.; Lauer, U. A.; Schick, F. *Magnetic Resonance in Medicine* **2005**, *54*, 231.

(54) Lauffer, R. B. *Chemical Reviews* **1987**, *87*, 901.

(55) Aime, S.; Botta, M.; Fasano, M.; Terreno, E. *Chemical Society Reviews* **1998**, *27*, 19.

(56) Que, E. L.; Chang, C. J. *Chemical Society Reviews* **2010**, *39*, 51.

(57) Aime, S.; Botta, M.; Crich, S. G.; Giovenzana, G.; Pagliarin, R.; Sisti, M.; Terreno, E. *Magnetic Resonance in Chemistry* **1998**, *36*, S200.

(58) Bottrill, M.; Nicholas, L. K.; Long, N. J. *Chemical Society Reviews* **2006**, *35*, 557.

(59) Lowe, M. P. *Australian Journal of Chemistry* **2002**, *55*, 551.

(60) Smart, L. E.; Moore, E. A. *Solid State Chemistry: An Introduction*, 3rd ed.; Taylor & Francis group: Florida, 2005.

(61) West, A. R. *Basic Solid State Chemistry*, 2nd ed.; John Wiley & Sons Sussex, 1999.

(62) Koylu, Z. K.; Asubay, S.; Yilmaz, A. *Molecules* **2009**, *14*, 1537.

(63) Fischer, A. E.; Hall, L. D. *Magnetic Resonance Imaging* **1996**, *14*, 779.

(64) Graedel, T. E. *Corrosion Science* **1987**, *27*, 741.

(65) Graedel, T. E. *Journal of the Electrochemical Society* **1987**, *134*, C109.